AERODYNAMIC MIXING LOSSES AND DISCHARGE COEFFICIENTS DUE TO FILM COOLING FROM A SYMMETRIC TURBINE AIRFOIL IN TRANSONIC FLOW

by

Dale Jay Jackson

A thesis submitted to the faculty of
The University of Utah
In partial fulfillment of the requirements of the degree of

Master of Science

Department of Mechanical Engineering

The University of Utah

December 1998

THE UNIVERSITY OF UTAH GRADUATE SCHOOL

SUPERVISORY COMMITTEE APPROVAL

of a thesis submitted by

Dale Jay Jackson

This thesis has been read by each member of the following supervisory committee and by majority vote has been found to be satisfactory.

16 July 1998

Chair: Phillip M. Ligrani

15/7/98

Gary Sandquist

16 Jul 98

James K. Strozier

THE UNIVERSITY OF UTAH GRADUATE SCHOOL

FINAL READING APPROVAL

To the Graduate Council of the University of Utah:

I have read the thesis of Dale Jay Jackson in its final form and have found that (1) its format, citations, and bibliographic style are consistent and acceptable; (2) its illustrative materials including figures, tables, and charts are in place; and (3) the final manuscript is satisfactory to the supervisory committee and is ready for submission to The Graduate School.

16 July 1998
Date

Phillip M. Ligrani
Chair, Supervisory Committee

Approved for the Major Department

Stephen R. Swanson
Acting Chair

Approved for the Graduate Council

Ann W. Hart
Dean of The Graduate School

ABSTRACT

Aerodynamic losses and discharge coefficients are obtained for two different Pratt and Whitney axisymetric turbine airfoils with film cooling holes. Blade 3 results are given for the blowing ratios, of 0.42, 0.73, and 1.28. The pressure ratios are 1.18, 1.45, and 2.07 for the "ambient" tests and 1.12, 1.19, and 1.78 for the "cold" tests. The density ratios are 0.840, 0.88, and 0.973 for the "ambient" tests and 1.130, 1.37, and 1.330 for the "cold" tests. Blade 4 results are given for the blowing ratios, of 0.248, 0.39, and 0.697. The pressure ratios are 1.197, 1.357, and 1.876 for the "ambient" tests and 1.153, 1.305, and 1.607 for the "cold" tests. The density ratios are 0.838, 0.867, and 0.95 for the "ambient" tests and 1.032, 1.127, and 1.223 for the "cold" tests.

Results of qualification tests of the Transonic Wind Tunnel are also given. These include test section inlet uniformity, flow variation with time, Schlerien images of the test section flow, and the Mach number distribution along the surface of the airfoil. All tests indicate satisfactory test section and wind tunnel preformance.

The integrated aerodynamic losses for Blade 3 range between .0383 and 0.51 for the "ambient" tests and between 0.411 and 0.507 for the "cold" tests. For Blade 4, the integrated aerodynamic losses range from 0.525 and 0.55 for the "ambient" tests and 0.495 and 0.538 for the "cold" tests. Integrated aerodynamic losses are generally lower with "cold" injection than with "ambient" injection for Blade 3. Blade 3 gives lower integrated aerodynamic losses compared to blade 4 when compared at the same Mach number ratio. This is attributed to the different film hole geometries of the blades.

The discharge coefficients associated with the film holes on Blade 3 range from 0.94 to 1.3 for "ambient" tests and 1.07 to 1.3 for "cold" tests. The discharge coefficients associated with the film holes on Blade 4 range from 0.54 to 0.78 for "ambient" tests and 0.55 to 0.80 for "cold" tests. Hole diameters used to calculate discharge coefficients are 0.381 mm and 0.469 mm for blades 3 and 4, respectively. These diameters account for some discharge coefficient values greater than one. In all cases, discharge coefficients increase as the pressure ratio increases, and discharge coefficients measured with freestream cross flow are generally lower than values measured with no freestream cross flow, for pressure ratios less than about 1.5, when compared at the same pressure ratio.

TABLE OF CONTENTS

LIST OF FIGURES

NOMENCLATURE

A	area
μ	absolute viscosity
c	blade chord
C	conic velocity
C_D	discharge coefficient
d	injectant hole diameter
ρ	density
k	ratio of specific heats
M	Mach number
m	mass flow rate
P	pressure
Re_∞	free stream Reynolds number based on blade chord
Re_c	injectant Reynolds number based on injectant hole diameter
R	gas constant
α	recovery factor
T	temperature
U	velocity
V	volumetric flow rate
Y	yaw pressure

Subscripts

B	bottom
c	injectant at the exit plane of the holes
e	exit of test section
∞	freestream
h	horizontal
i	inlet of test section
L	left
l	linear moving
m	actual static injectant conditions at rotameter location
n	normalized
O	standard static injectant conditions at rotameter location
p	injectant within plenum
r	recovery
R	right
s	static
T	top
t	total or stagnation
corr	corrected value
ideal	ideal isentropic value

ACKNOWLEGEMENTS

I would like to thank Dr. Phil Ligrani for his support and guidance on this project over the past year. Thanks also goes to Pratt and Whitney of West Palm Beach Florida especially Dr. P. Dean Johnson, Dr. Fred Soechting, Mr. Doug Hayes and Dr. Bill Kavasnick.

Thanks also to my fellow colleagues for their help, support, friendship, and patience while completing my research over the past year.

Greatest thank go to my Heavenly Father, family, and especially my dear wife Stacy.

CHAPTER 1

INTRODUCTION

This chapter gives background on the study, discusses prior work, and describes thesis organization.

1.1 Background

The idea of jet propulsion is thought to have come from a man named Hero who lived in Alexandria, Egypt, around 150 BC. He invented a novelty toy driven by steam that he called an aeolipile. An illustration of this aeolipile is seen in Figure 1.1.

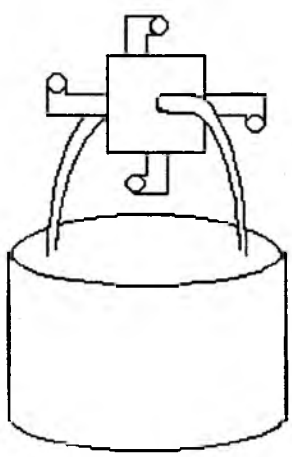

Figure 1.1 The Hero steam engine.

The historical records are not precise in describing the aeolipile. If Hero's device resembled the illustration above then it was a primitive form of a jet engine. The heating of air in a vertical tube induced a flow of air in several tubes arranged radially around a horizontal wheel, and rotation resulted from the creation of an impulse effect.

The gas turbine engine is essentially a heat engine using air as a working fluid to provide thrust. To achieve this the air passing through the engine has to be accelerated. First, the pressure energy is raised, followed by the addition of heat energy, and then the energy is converted back into kinetic energy in the form of a high velocity jet.

The basic mechanical arrangement of a gas turbine is relatively simple. It consists of four major sections, the compressor that raises the pressure energy, the combustion chambers in which the heat energy is introduced, the turbine that converts some of the energy into rotational energy to drive the compressor, and the nozzle that accelerates the air producing the high velocity jet exhaust. This generalization does not take into account all of the detailed components in each of the engine sections. A schematic drawing of a gas turbine engine is shown in Figure 1.2.

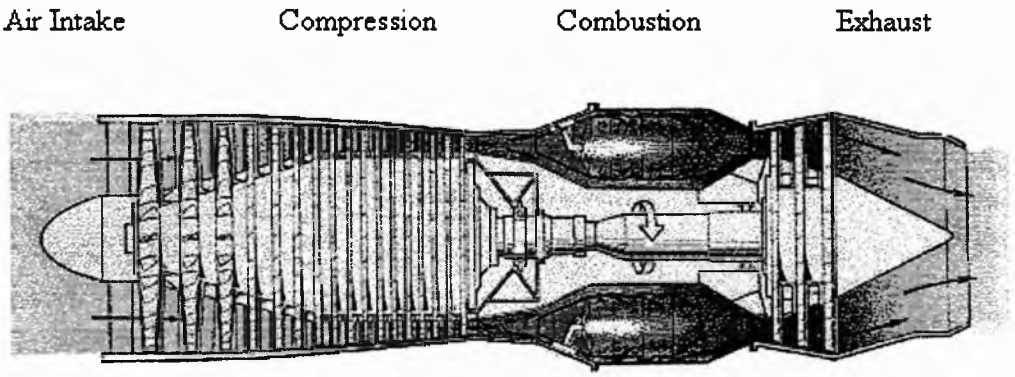

Figure 1.2 A schematic of a gas turbine engine.

All parts in the engine are necessary for the gas turbine to operate. The part of the engine that is the focus of the present study is the turbine. The turbine provides power to drive the compressor and accessories. It does this by extracting energy from the hot gases released from the combustion section and expanding them to a lower pressure and temperature. The continuous flow of gas to which the turbine is exposed may enter the turbine at temperatures varying between 850 °C and 1900 °C. Higher temperatures in this range exceed the melting points of current turbine materials.

The turbine consists of many stages. Each stage consists of a row of stationary blades called stators, and a row of rotating blades called rotors. The number of stages depends on the relationship between the power required from the gas flow, the rotational speed, and the diameter of the turbine rotor.

In order to produce high engine efficiency, the air at the inlet of the turbine must be as hot as possible. The hotter the gas, the better the engine efficiency. Because turbine blades are required to operate for long periods at temperatures above the melting points of the materials employed, film cooling is required to cool turbine blade surfaces. A photograph of a turbine blade with film cooling holes is shown in Figure 1.3.

Figure 1.3 A turbine blade with film cooling holes.

1.2 Prior Work

There is little other work reported in the literature on film cooling and discharge coefficients in transonic flow. Some of these studies are now described.

1.2.1 Transonic and High Subsonic Wake Studies

Mee et al. (1992) show the results from testing a set of nine blades each with a 100mm (3.9 in) true chord and a span of 300 mm (11.8 in). Exit Mach numbers range from 0.5 to 1.15 and Reynolds numbers range from 450,000 to 2,000,000. The overall losses from a transonic turbine cascade are due to individual contributions of boundary layer loss, shock loss, and mixing loss. The majority of the mixing loss is found immediately downstream of the trailing edge of the blade, where the largest property gradients can be found. Kapteijn and Amecke (1994) give information on wake losses using a cascade of turbine blades and inlet Mach numbers ranging from 0.7 to 1.2. Results show that pressure side ejection mixing takes place quicker than trailing edge ejection in subsonic flow. Vlasic et al. (1995) describe results from a high-work single-stage research turbine with pressure ratio of 5.0 and a stage loading of 2.2. The facility is a cold flow rig. Cooling the stator and rotor blades affects the overall efficiency by 2.1%. Ames and Plesniak (1997) preformed a study on airfoils that are 4.5 times scale C3X vanes. The vanes are taken from the first stage of a helicopter engine. The vanes true chord length is 14.493 cm (5.7 in), with an axial chord of 7.816 cm (3.08 in). The vane spacing is 11.773 cm (4.64 in) and the passage has a throat of 3.292 cm (1.3 in). A strong correlation between turbulence and the losses is described by the authors.

1.2.2 Shaped Hole Film Cooling Studies at Low Speeds

Wittig et al. (1996) describe the results measured downstream of simple round holes, lateral expanded shaped holes, and lateral expanded laid back shaped holes oriented with different angles to the crossflow. Shaped hole inclinations are 30 degrees, whereas round hole inclinations are 30, 45, and 90 degrees. At high pressure ratios, a maximum point of 0.87 is reached, independent of the crossflow Mach number. Thole et al. (1996) describe flow field measurements downstream of different film hole geometries, including round holes, laterally expanded holes, and forward-laterally expanded holes. The laterally expanded hole geometry reduces the penetration of the cooling jets relative to the round holes. Hyams et al. (1997) investigate five different hole geometries at blowing ratios of 1.25 and 1.88 and with a density ratio of 1.6. The hole configurations are cylindrical, forward-diffused, laterally-diffused, inlet-shaped, and cusp-shaped. The laterally-diffused film cooling holes provide the best coverage and highest effectiveness. The forward diffused holes work well along their centerlines but do not diffuse laterally. All of the other hole configurations produce coolant lift-off from the test surface. Brittingham et al. (1997) describe the performance of cylindrical holes inclined at 35°, 15° forward diffused holes inclined at a 60° compound angle, and 12° laterally diffused holes inclined at a 45° compound angle. Length to diameter ratio is 4.0, density ratio is 1.55, pitch to diameter ratio is 3.0, and film hole Reynolds number is 17350. Hole shaping results in lower pressure gradients in the area of the injectant breakout relative to the round holes. Dibbon et al. (1997) examine cylindrical holes at two different film hole length to diameter ratios, 1.75 and 3.5, and three different blowing ratios ranging from 0.5 to 2.0. Density ratio is 2.0 and injection angle is 35 degrees.

According to these investigations, the counter rotating secondary flow structure downstream of the jet exit is the most significant mechanism affecting the film cooling performance. McGovern et al. (1997) study film cooling from cylindrical holes with compound angle injection angles of 45, 60, and 90 degrees. Blowing ratios are 1.25 and 1.88, and the density ratio is 1.6. They indicate that compounding improves the lateral uniformity of the adiabatic effectiveness.

1.2.3 Discharge Coefficients

Hay et al. (1982) show that discharge coefficients reach maximum values ranging from 0.7 to 0.97 as the pressure ratio increases. Mach numbers range from 0 to 0.4. Cylindrical hole length to diameter ratios of 2 and 6 and hole inclinations of 30, 60, and 90 degrees are investigated. Hay et al. (1992) present results taken from round cylindrical holes inclined at 30° and a cross flow with Mach numbers of 0, 0.15, and 0.3. Five different hole orientations to the flow direction are studied. Lower discharge coefficients are measured with an increase in the angle of orientation of the holes. Hay et al. (1995) describe the effects of discharge coefficients from flared film cooling holes. The holes are inclined at 30 and 90 degrees with external cross flow Mach numbers of 0.15 and 0.3. Discharge coefficients of flared holes are higher than the ones determined for round holes when compared at the same pressure ratio. This means that flared holes produce a smaller pressure drop at a particular flow rate.

1.3 Present Study

The present study focuses on mixing losses associated with film cooling from the surfaces of two different symmetric transonic turbine blades. Contoured top and bottom

walls provide the pressure gradients and Mach number distributions along the blade surfaces which match values along suction surfaces of turbine blades in the first stages of operating engines. The freestream Mach number along the blade surface ranges from 0.4 to 1.2. A secondary air injection system is used to provide film cooling at different blowing ratios and at different density ratios. Discharge coefficients are also measured for both film hole geometries tested at different film density ratios and different film blowing ratios.

1.4 Thesis Organization

Here, in Chapter 1, an introduction is given. Chapter 2 discusses the experimental apparatus and procedures. Chapter 3 describes different qualification tests of the experimental apparatus and procedures. Chapter 4 presents the theoretical considerations of the study. Chapter 5 shows the experimental results. Finally, Chapter 6 gives the summary and conclusions.

CHAPTER 2

EXPERIMENTAL APPARATUS AND PROCEDURES

This chapter describes test apparatus components, and experimental procedures. The first section deals with the experimental equipment, and the devices used to acquire the experimental data. The next section deals with the safety features of the apparatus.

2.1 Equipment and Setup

2.1.1 Main Air Flow Line

Figure 2.1 shows a schematic diagram of the test facility. Figure 2.2 shows a photograph of the compressor. The compressor is model RL-1155-CB made by the Gardner and Denver Company. This model is a 74.6 kW (100 hp) unit which produces compressed air up to 2.4 MPa (350 psig). The air travels from the compressor to the storage tanks through a series of dryers and filters. The storage tanks are an array of 8 tanks each having the capability to store 68.9 MPa (10000 psig). The total amount of storage volume held by these 8 tanks is 11.9 m^3 (424 ft^3). Figure 2.3 shows the end view of these 8 tanks along with the octopus manifold that combines the air from each tank into one 25.4 cm (10 inch) line.

Figure 2.4 shows the Fisher regulator that is operated by an electronic controller to regulate the main air supply. The Fisher regulator is made up of a 6X4 EWT design

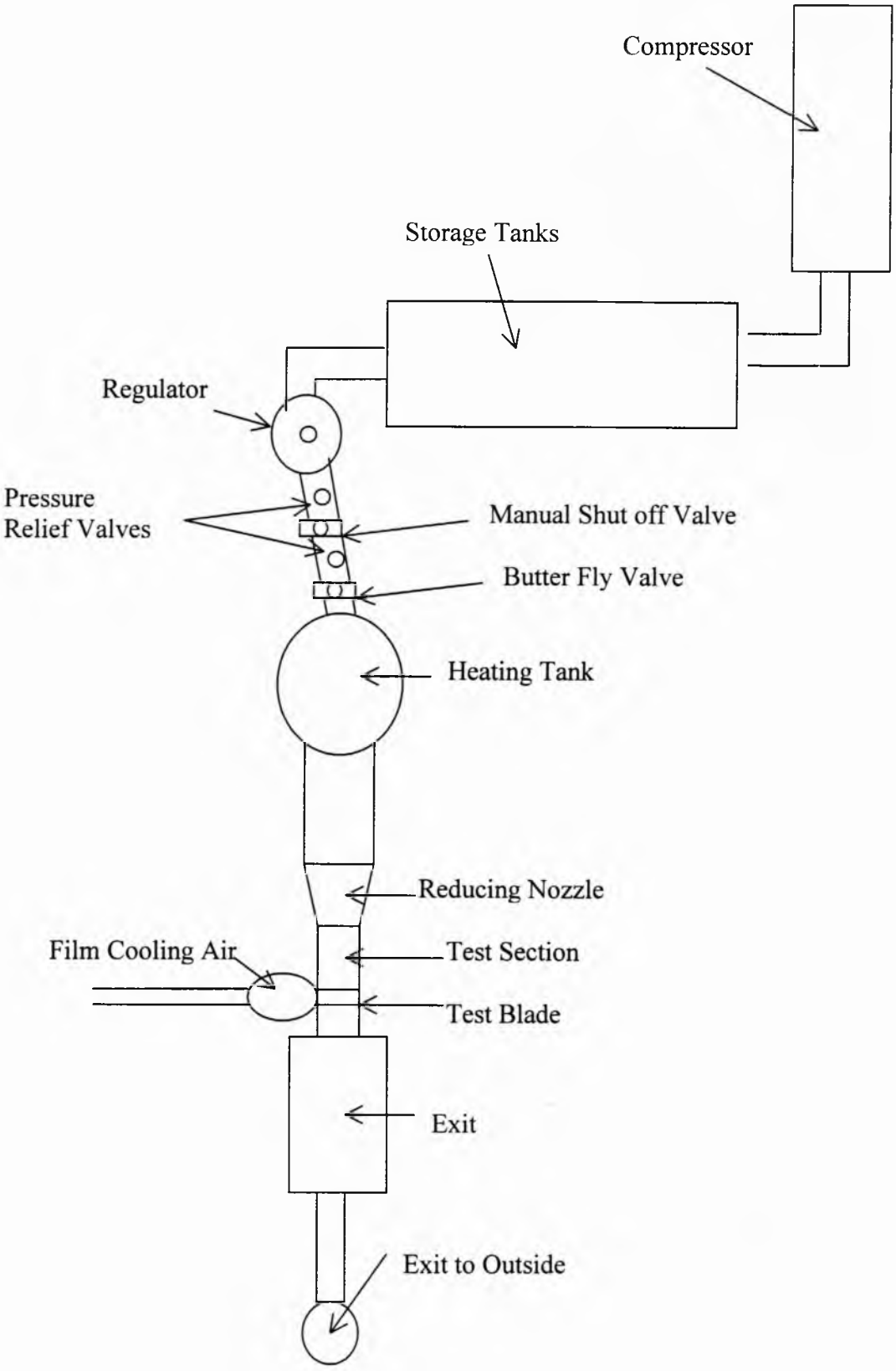

Figure 2.1 Test facility setup.

Figure 2.2 Air compressor.

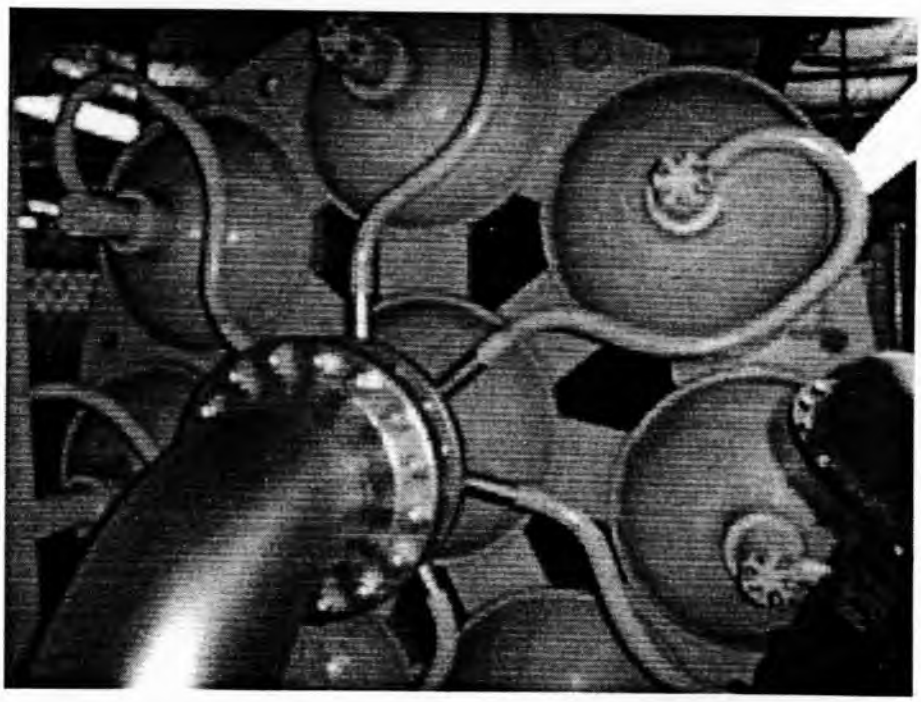

Figure 2.3 Storage tanks and octopus manifold.

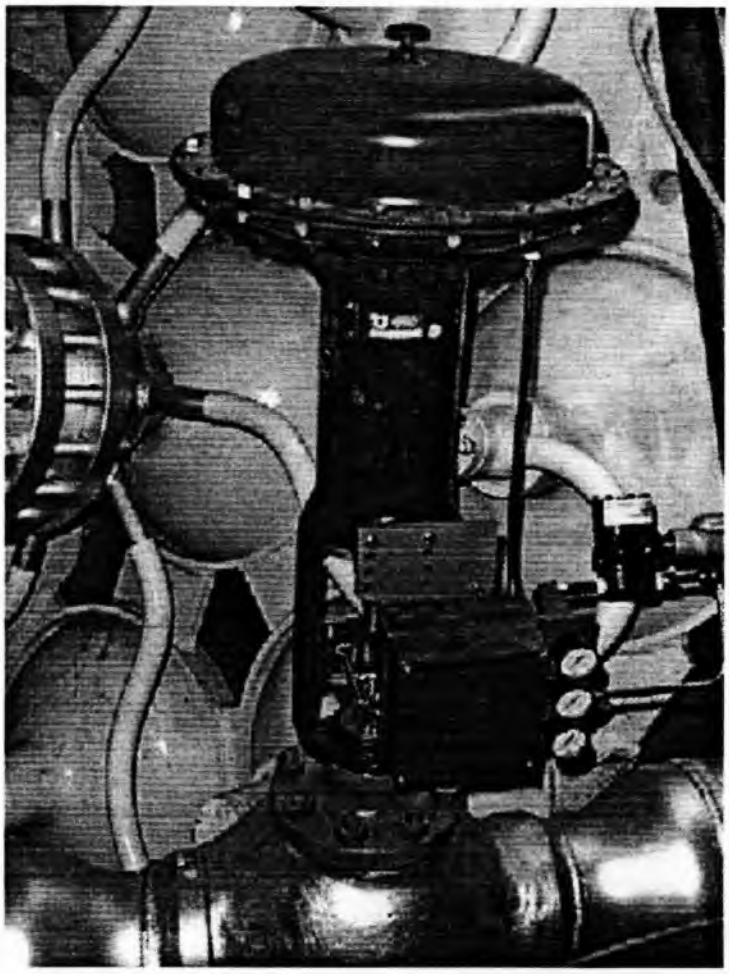

Figure 2.4 Fisher pressure regulator.

sliding gate valve, a 3582 series valve positioner, and a type 667 diaphragm actuator. A Powers Process Controls 385 ¼ DIN controller operates this regulator.

The control board is shown in Figure 2.5 and contains a conglomerate of gauges showing storage tank pressure, line pressure just down stream of the Fisher regulator, line pressure just upstream of the test section, and other gauges. The readout and switch control for the Powers 535 pressure controller is also found on this control board.

The Powers 535 pressure controller is an electronic multi option process controller. The controller enables four different types of pressure control to be implemented:

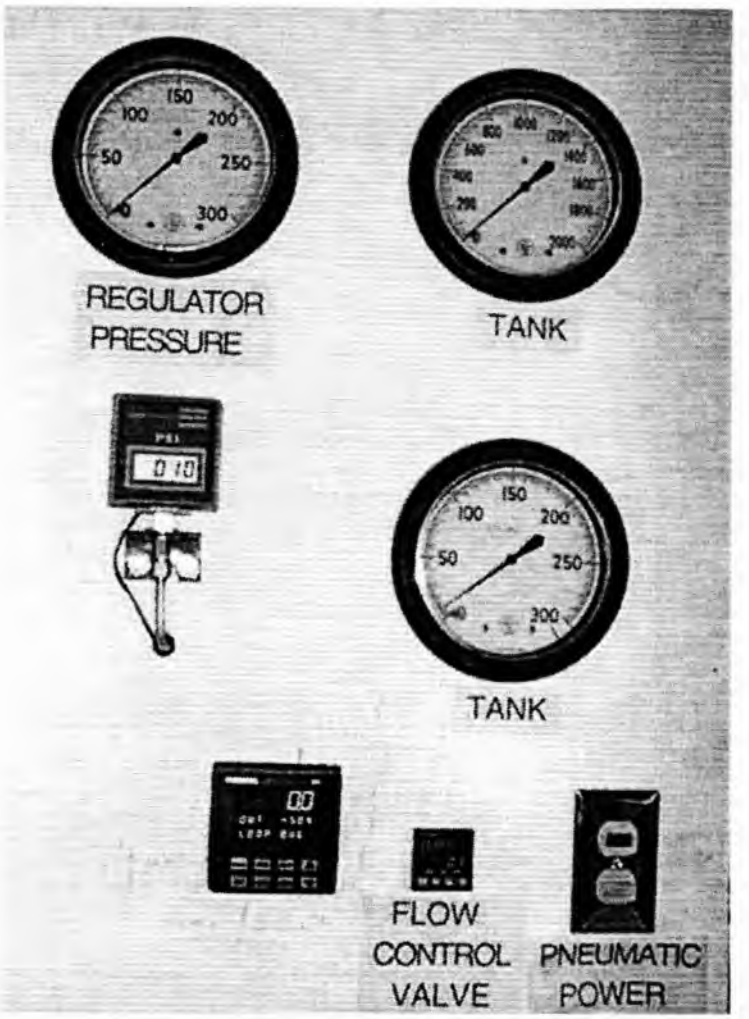

Figure 2.5 Control panel.

proportional (P), proportional with derivative (PD), proportional with integral (PI), and proportional with derivative and integral (PID). For the experiments performed as part of this thesis, the PI setting is used with the set point at 296.5 kPa (43 psig), the proportional set at 85%, and the integral set at 150%. The Powers 535 controller receives a milliamp input, which is proportional to the static pressure located just down stream of the Fisher regulator, from a WKA Tronic Line Pressure Transmitter 891.13.500, shown in Figure 2.6. The pressure controller then processes the air flow according to the readings from

Figure 2.6 Pressure gauge.

this transmitter and the electronic controller setting. The controller then sends out a milliamp signal to the Bellofram 961-070-000 T-1000 electronic pressure regulator controller. The electronic pressure regulator then sends air pressure to the Fisher 3582 valve positioner that actuates the Fisher 6X4 EWT sliding gate valve. Down stream of the Fisher regulator are two Kunkle relief valves and a manual shutoff valve. These devices are discussed later in the safety part of the chapter.

The heating tank follows, but is not used for heating in these experiments, but rather as a plenum. The heating tank is 91.4 cm (36 inch) in diameter, 251.4 cm (99 inch)

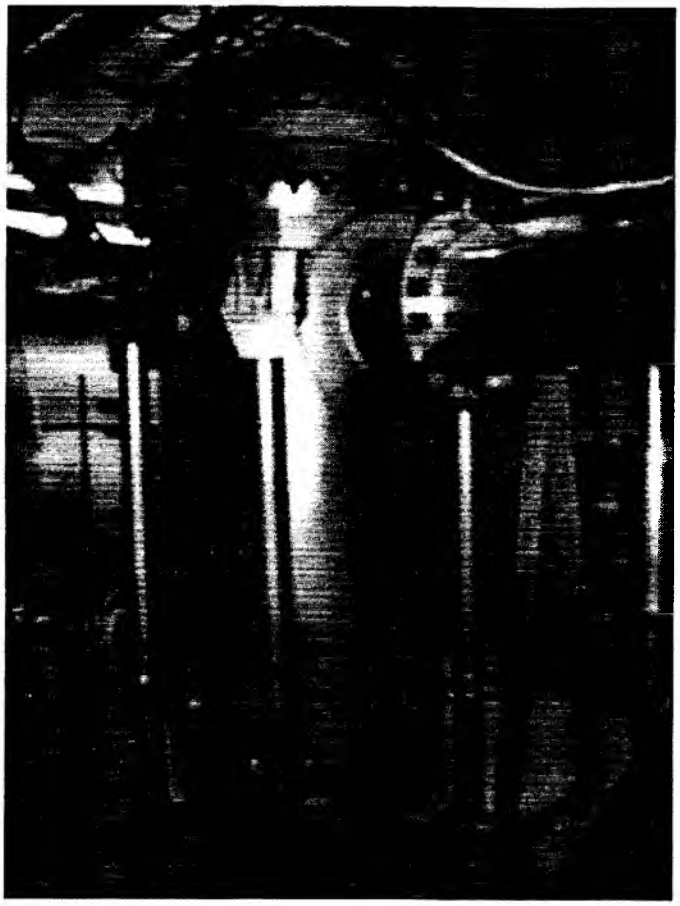

Figure 2.7 Heater tank.

in height, and composed of 1.27 cm (1/2 inch) steel plate. Figure 2.7 shows the heater tank.

The ducting from the heating tank to the test section consists of 30.48 cm (12 inch) straight pipe, a round to square adapter, and a nozzle. Figures 2.8 and 2.9 show the adapter and reducing nozzle, respectively. The adapters round end fits to the 30.48 cm (12 inch) pipe and has square end dimensions of 26.27 cm (10.5 inch) by 26.27 cm (10.5 inch). The nozzle was designed using a fifth order polynomial and is 60.96 cm (24 inch) long. The nozzle converges from the 26.27 cm (10.5 inch) square to a 12.7 cm (5 inch) square. Table 2.1 gives the contour coordinates of the nozzle, where X is measured from

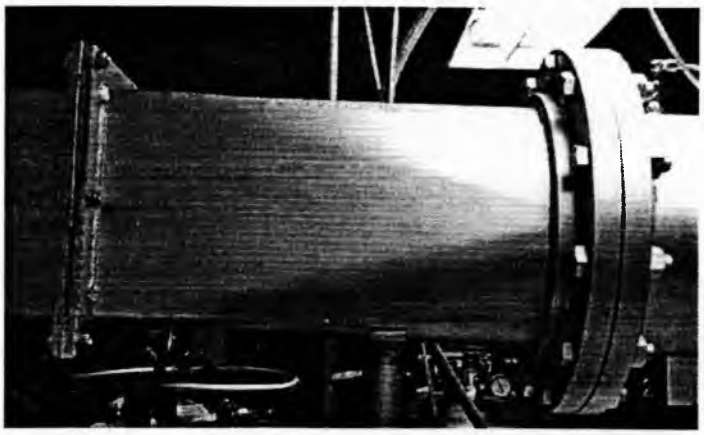

Figure 2.8 Round to square pipe adapter.

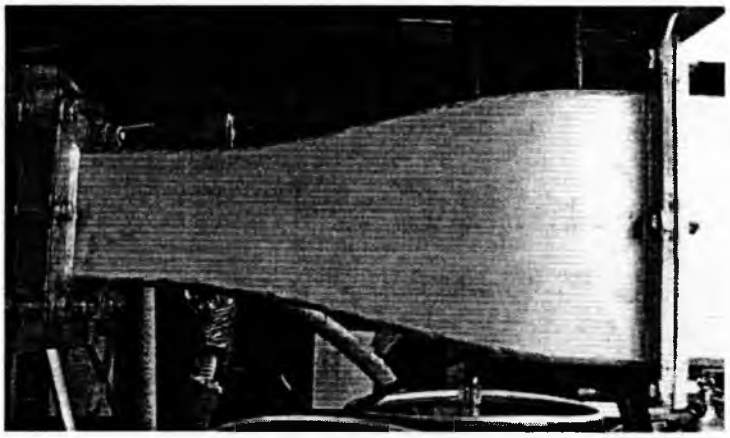

Figure 2.9 Reducing nozzle.

the nozzle inlet, and Y is measured from the center line to the inner wall of the nozzle. This design minimizes the likelihood of flow separation, separation bubbles, and vortices from the boundary layers developing along the concave nozzles surfaces.

Following the nozzle is the test section. Figure 2.10 and 2.11 show the test section with a symmetric turbine blade installed. The test section is made of 3.175 cm (1.25 inch) thick acrylic and consists of a top wall, a bottom wall, right and left side walls and two transition flanges to connect to the reducing nozzle and the exit plenum. The test

Table 2.1 Nozzle contour coordinates.

X (cm)	Y (cm)
5.08	13.3350
10.16	13.3350
15.24	13.3350
20.32	12.0650
25.40	11.4300
30.48	10.1600
35.56	9.5250
40.64	8.8900
45.72	7.9375
50.80	6.9850
55.88	6.3500
60.96	6.3500

section also has two specially made stainless steel, top and bottom wall inserts that accelerate the air in the test section from Mach .2 at the test section inlet to Mach 1.2 at the trailing edge of the test blade. Table 2.2 shows the top and bottom wall insert contour coordinates. The X coordinates are measured from the upstream edge of the top and bottom walls and the Y coordinated are referenced to the centerline of the test section. The test blades are contoured to produce the same static pressure distribution and Mach number distribution as on the suction surface of the turbine blades in the first stage of an operating transonic gas turbine engine. Table 2.3 gives the coordinates of the test blade with respect to the test section inlet. Figure 2.12 shows a plot of the airfoil coordinates, and the contoured top and bottom wall coordinates.

The plenum shown in Figure 2.13 follows the test section. The air within the plenum decelerates the flow and decreases the pressure from 193 kPa (28 psia) to 85.5 kPa (12.4 psia, ambient pressure). The plenum dimensions are 92.71 cm (36.5 inch) by91.44 cm (36 inch) by 91.44 cm (36 inch). The plenum is lined with 5.0 cm (2 inch)

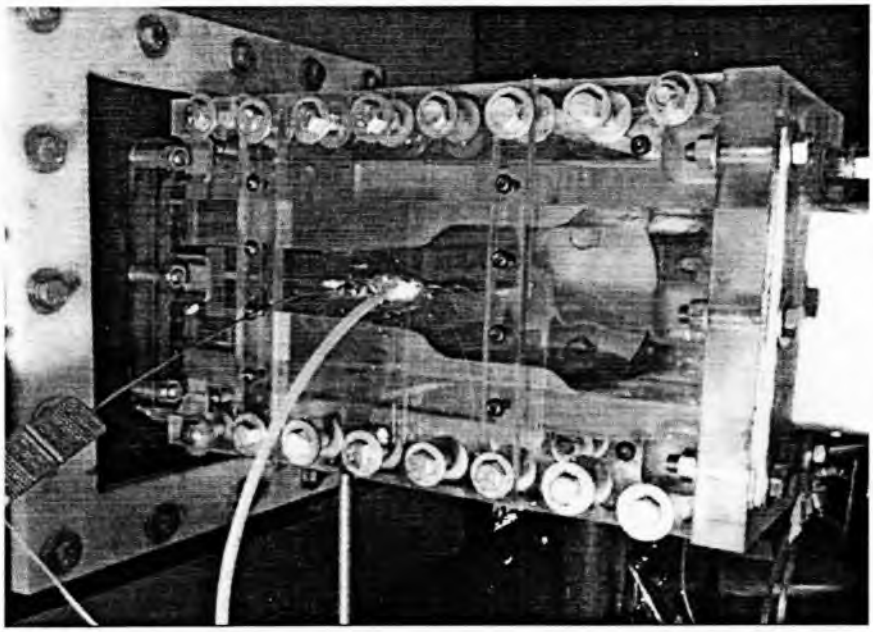

Figure 2.10 Test section with blade installed A (full view).

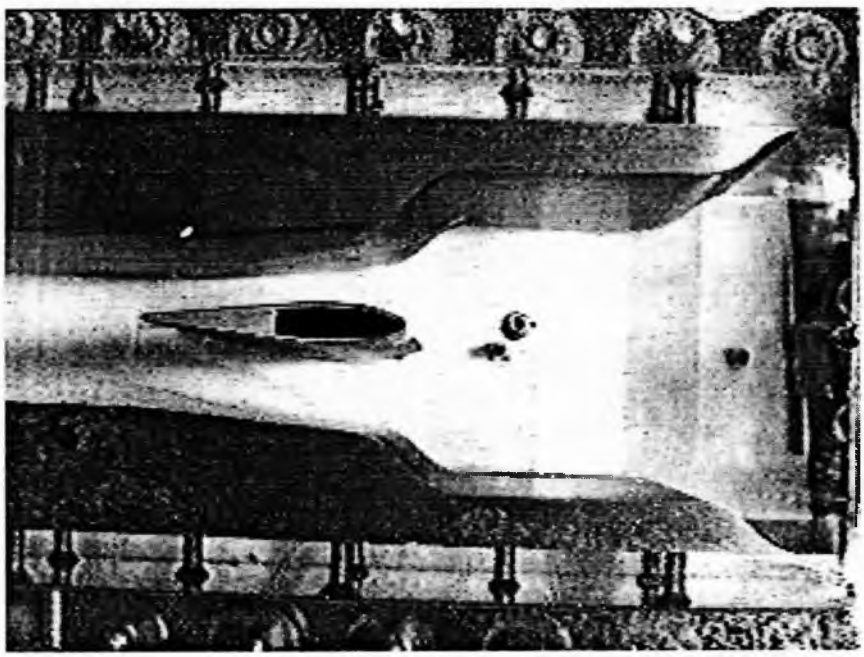

Figure 2.11 Test section with blade installed B (close-up view).

Table 2.2 Top and bottom wall contour coordinates with respect to test section entrance.

X (cm)	Y (cm)	-Y (cm)	X (cm)	Y (cm)	-Y (cm)	X (cm)	Y (cm)	-Y (cm)
9.508	6.350	-6.350	16.704	4.814	-4.814	23.791	3.001	-3.001
9.838	6.328	-6.328	17.035	4.814	-4.814	24.121	2.973	-2.973
10.163	6.264	-6.264	17.366	4.814	-4.814	24.451	2.945	-2.945
10.476	6.158	-6.158	17.697	4.814	-4.814	24.781	2.917	-2.917
10.773	6.013	-6.013	18.028	4.814	-4.814	25.110	2.889	-2.889
11.049	5.830	-5.830	18.359	4.814	-4.814	25.440	2.862	-2.862
11.298	5.612	-5.612	18.690	4.814	-4.814	25.770	2.834	-2.834
11.540	5.387	-5.387	19.021	4.814	-4.814	26.100	2.806	-2.806
11.810	5.195	-5.195	19.352	4.814	-4.814	26.430	2.778	-2.778
12.102	5.040	-5.040	19.683	4.814	-4.814	26.760	2.750	-2.750
12.411	4.923	-4.923	20.012	4.784	-4.784	27.089	2.722	-2.722
12.734	4.848	-4.848	20.335	4.711	-4.711	27.419	2.694	-2.694
13.063	4.816	-4.816	20.646	4.598	-4.598	27.749	2.666	-2.666
13.394	4.814	-4.814	20.939	4.444	-4.444	28.079	2.638	-2.638
13.725	4.814	-4.814	21.210	4.254	-4.254	28.409	2.612	-2.612
14.056	4.814	-4.814	21.454	4.031	-4.031	28.739	2.589	-2.589
14.387	4.814	-4.814	21.677	3.787	-3.787	29.070	2.571	-2.571
14.718	4.814	-4.814	21.925	3.568	-3.568	29.400	2.556	-2.556
15.049	4.814	-4.814	22.199	3.383	-3.383	29.731	2.547	-2.547
15.380	4.814	-4.814	22.495	3.235	-3.235	30.062	2.541	-2.541
15.711	4.814	-4.814	22.808	3.127	-3.127	30.393	2.540	-2.540
16.042	4.814	-4.814	23.132	3.060	-3.060	44.958	2.540	-2.540
16.373	4.814	-4.814	23.461	3.029	-3.029	-	-	-

foam to dampen the vibrations produced by the exiting air. The inside of the plenum is shown in Figure 2.14. As evident from this photograph, the plenum contains traversing motors, a pitot-static probe, a thermocouple, and pressure transducers. Three exit pipes from the plenum are seen in Figure 2.15. Two of the exit pipes join together at the top of the plenum. These pipes exit from the roof of the Merrill Engineering building and operate to maintain the plenum near atmospheric pressure during all blow down runs of the facility.

Table 2.3 Airfoil coordinates with respect to the test section inlet.

X (cm)	Y (cm)	-Y (cm)	X (cm)	Y (cm)	-Y (cm)	X (cm)	Y (cm)	-Y (cm)
21.62	0.00	0.00	24.10	0.57	-0.57	26.72	0.32	-0.32
21.64	0.07	-0.07	24.17	0.57	-0.57	26.80	0.31	-0.31
21.67	0.13	-0.13	24.24	0.56	-0.56	26.87	0.31	-0.31
21.73	0.17	-0.17	24.31	0.56	-0.56	26.94	0.30	-0.30
21.80	0.20	-0.20	24.38	0.56	-0.56	27.01	0.29	-0.29
21.86	0.23	-0.23	24.45	0.55	-0.55	27.08	0.28	-0.28
21.93	0.26	-0.26	24.52	0.55	-0.55	27.15	0.28	-0.28
21.99	0.29	-0.29	24.60	0.54	-0.54	27.22	0.27	-0.27
22.06	0.31	-0.31	24.67	0.54	-0.54	27.29	0.26	-0.26
22.13	0.34	-0.34	24.74	0.53	-0.53	27.36	0.25	-0.25
22.19	0.36	-0.36	24.81	0.52	-0.52	27.43	0.25	-0.25
22.26	0.38	-0.38	24.88	0.52	-0.52	27.51	0.24	-0.24
22.33	0.40	-0.40	24.95	0.51	-0.51	27.58	0.23	-0.23
22.40	0.42	-0.42	25.02	0.50	-0.50	27.65	0.22	-0.22
22.47	0.44	-0.44	25.09	0.49	-0.49	27.72	0.22	-0.22
22.54	0.46	-0.46	25.16	0.49	-0.49	27.79	0.21	-0.21
22.61	0.47	-0.47	25.23	0.48	-0.48	27.86	0.20	-0.20
22.68	0.49	-0.49	25.31	0.47	-0.47	27.93	0.20	-0.20
22.75	0.50	-0.50	25.38	0.46	-0.46	28.00	0.19	-0.19
22.82	0.51	-0.51	25.45	0.46	-0.46	28.07	0.18	-0.18
22.89	0.52	-0.52	25.52	0.45	-0.45	28.14	0.17	-0.17
22.96	0.53	-0.53	25.59	0.44	-0.44	28.21	0.17	-0.17
23.03	0.54	-0.54	25.66	0.43	-0.43	28.29	0.16	-0.16
23.10	0.55	-0.55	25.73	0.43	-0.43	28.36	0.15	-0.15
23.17	0.55	-0.55	25.80	0.42	-0.42	28.43	0.14	-0.14
23.24	0.56	-0.56	25.87	0.41	-0.41	28.50	0.14	-0.14
23.31	0.56	-0.56	25.94	0.40	-0.40	28.57	0.13	-0.13
23.38	0.56	-0.56	26.02	0.40	-0.40	28.64	0.12	-0.12
23.46	0.57	-0.57	26.09	0.39	-0.39	28.71	0.11	-0.11
23.53	0.57	-0.57	26.16	0.38	-0.38	28.78	0.11	-0.11
23.60	0.57	-0.57	26.23	0.37	-0.37	28.85	0.10	-0.10
23.67	0.57	-0.57	26.30	0.37	-0.37	28.92	0.09	-0.09
23.74	0.57	-0.57	26.37	0.36	-0.36	28.99	0.08	-0.08
23.81	0.57	-0.57	26.44	0.35	-0.35	29.07	0.08	-0.08
23.88	0.57	-0.57	26.51	0.34	-0.34	29.14	0.07	-0.07
23.95	0.57	-0.57	26.58	0.34	-0.34	29.21	0.06	-0.06
24.03	0.57	-0.57	26.65	0.33	-0.33	29.24	0.00	0.00

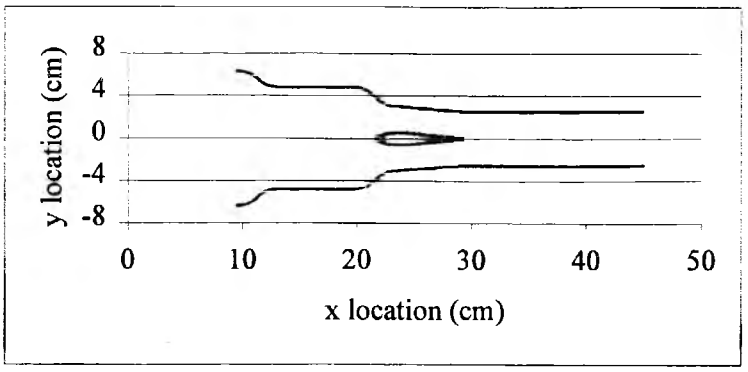

Figure 2.12 Test section contour with airfoil.

2.1.2 Film Cooling Air Flow Line

The secondary, film cooling air is produced by the system shown in Figure 2.16. The setup contains a particulate filter, regulator, sonic orifice, coalescing filter, air dryer, Dwyer volumetric flow meters, heat exchanger, liquid nitrogen tanks, pin valve, and a transition duct. Each of these parts plays an important role in the cooling air. The particulate filter removes large particles from the secondary air. The regulator controls and maintains the pressure of the air during a blow down run. The sonic orifice is next in line and is seen in Figure 2.17. The sonic orifice is used to measure the mass flow rate of the cooling air. The coalescing filter comes next and removes fine particles in the air just before the air dryer. The air dryer uses a desiccant and removes moisture form the air at temperatures as low as –100 ^{0}C. Figure 2.18 shows the Dwyer volumetric flow meters that are also used to measure the mass flow rate of the cooling air. The heat exchanger shown in Figure 2.19 is especially designed for low temperature heat transfer, and employs liquid nitrogen as a coolant. A pin valve, made for very low temperature operation, controls the liquid nitrogen flow, and is shown in Figure 2.20.

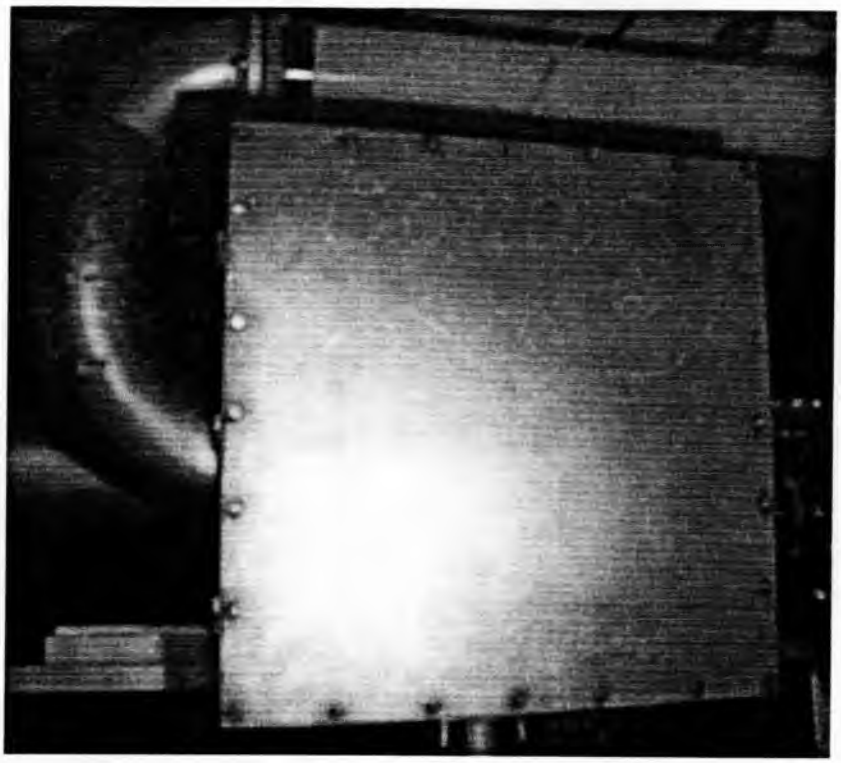

Figure 2.13 Exit plenum.

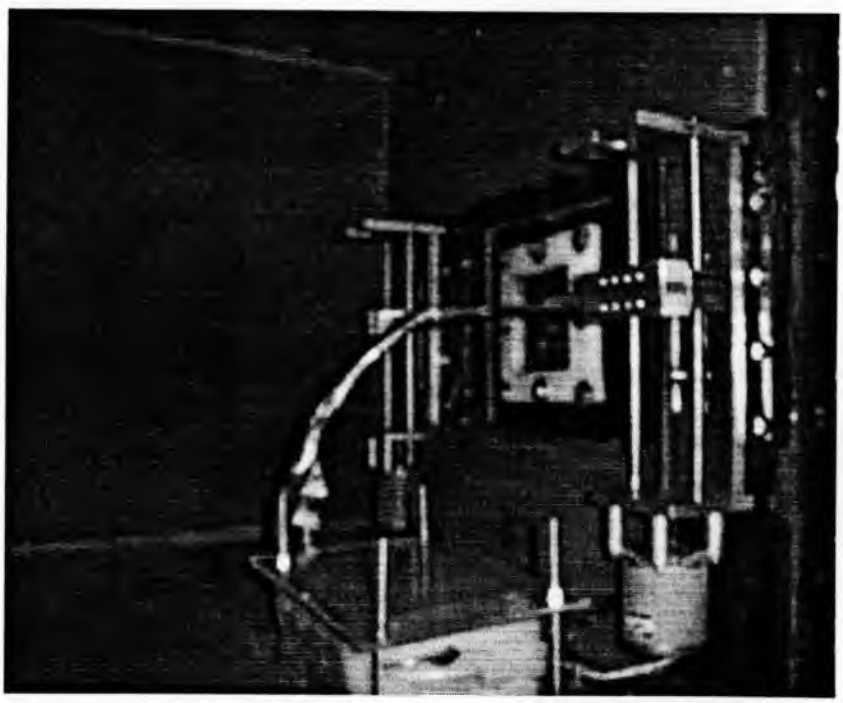

Figure 2.14 Inside of plenum.

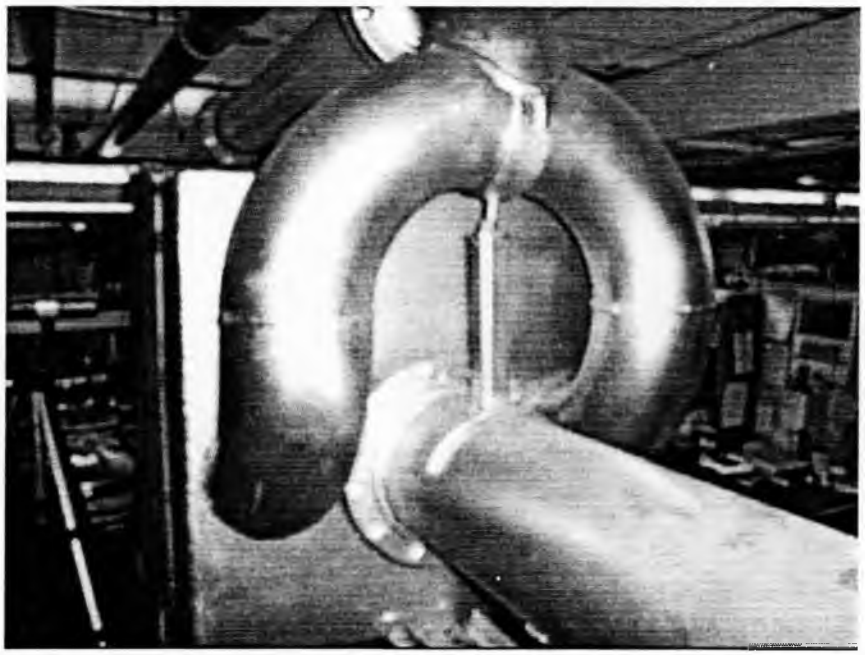

Figure 2.15 Exit pipes.

2.1.3 Measurement Devices

Figure 2.21 shows the Hewlett Packard 3497A data acquisition control unit and seven Celesco model number CD 10D Carrier Demodulators. The Carrier Demodulators are used to convert signals from the pressure transducers to a D.C. voltage that is sent to a Hewlett Packard 44422A data card located in the data acquisition control unit. The Hewlett Packard data acquisition components acquire the readings that are then sent to the computer, and stored for analysis. Seven pressures and five temperatures are acquired using these devices, as each blow down test is underway. The pressure transducers measure pressures from pitot-static probes and static ports located at the test

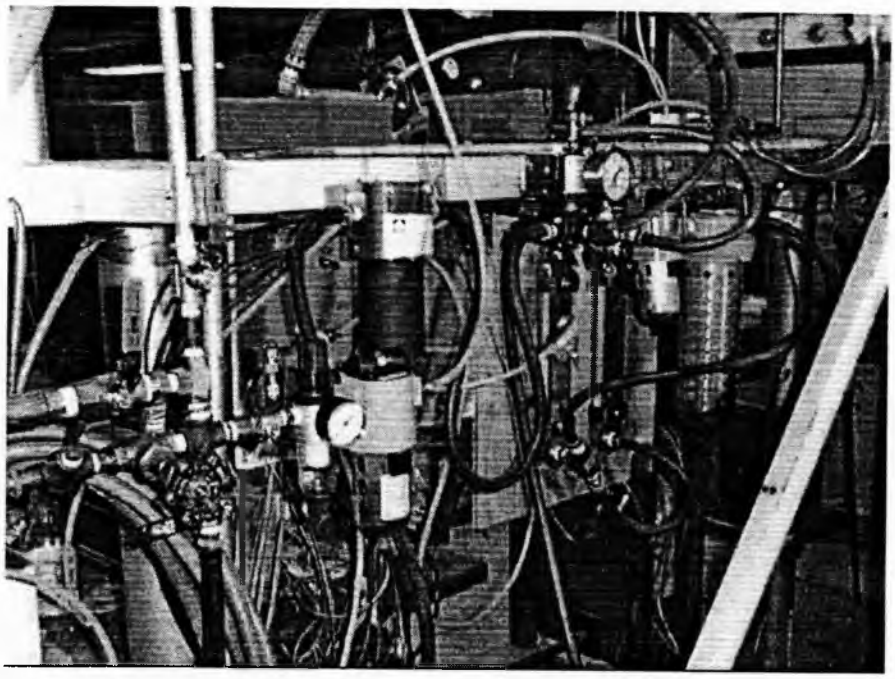

Figure 2.16 Film cooling air system.

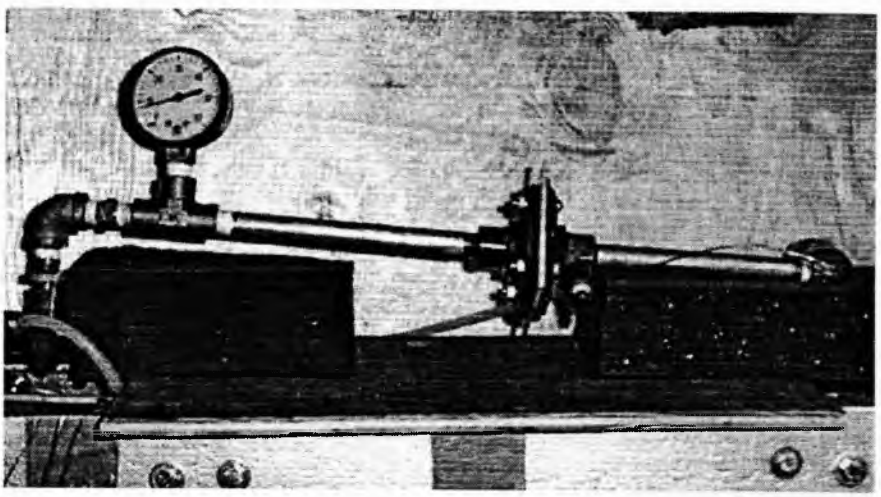

Figure 2.17 Sonic orifice.

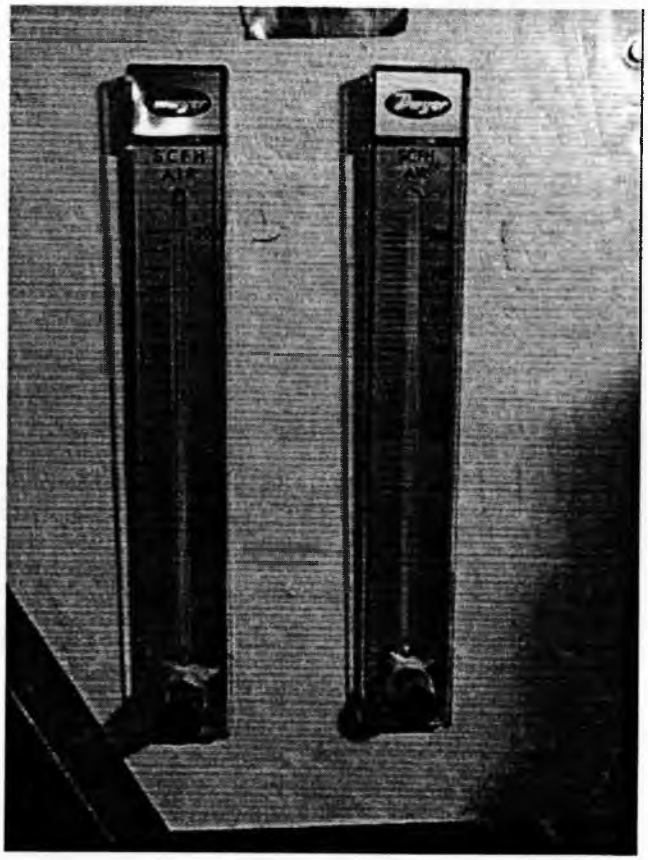

Figure 2.18 Dwyer volumetric flow meters.

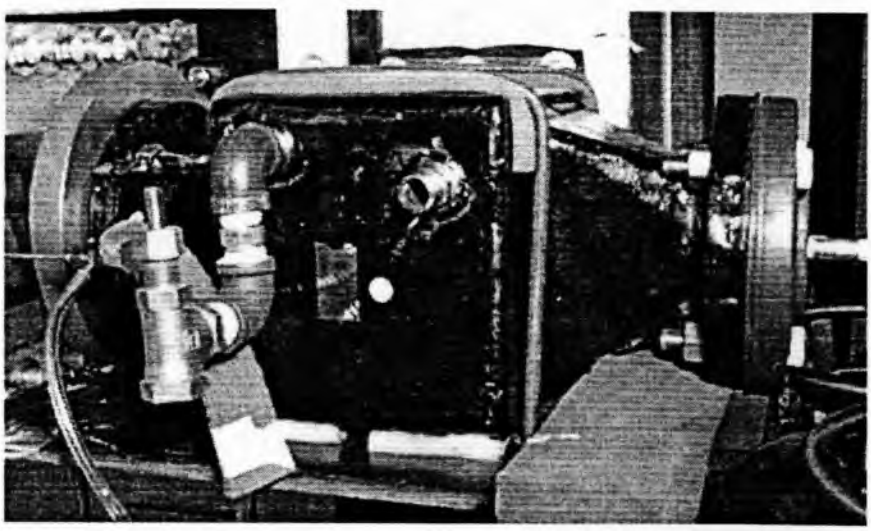

Figure 2.19 Heat exchanger.

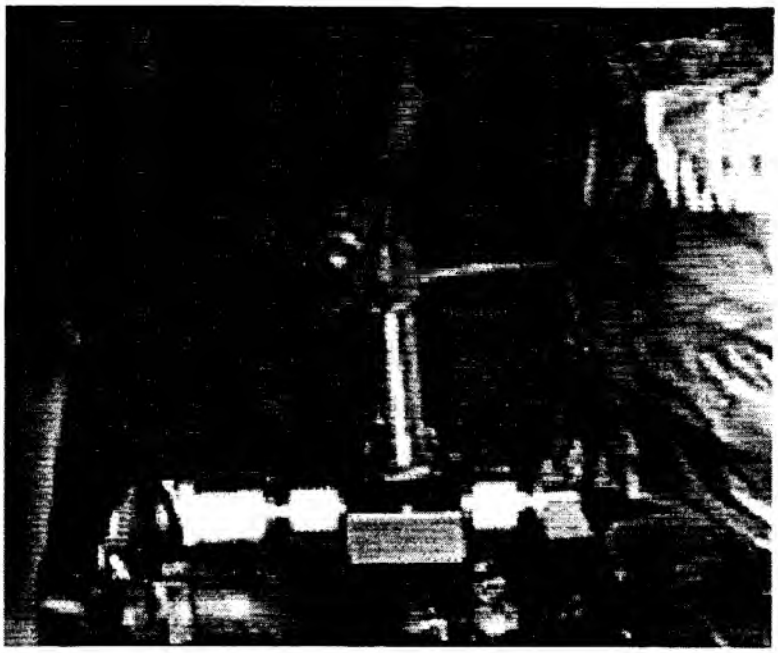

Figure 2.20 Liquid nitrogen pin valve.

section inlet, exit, and blade plenum. These pressures are the inlet static, inlet total, exit static, exit total, upstream of the sonic orifice, downstream of the sonic orifice, and static pressure within the plenum of the blade. Recovery temperatures at the test section inlet and exit, total temperature in the blade plenum, total temperature upstream of the sonic orifice, and ambient temperature are also measured. These pressures and temperatures are used to calculate Mach numbers, sonic velocities, mass flow rates, discharge coefficients, and many other useful items. Figure 2.22 shows the setup for the acquisition system. The exit static pressure, and exit total pressure, along with the exit recovery temperature are taken as the pitot-static probe and thermocouples are traversed through the wake of the test blade. The traversing mechanism consists of two Superior Electric SLO-SYN synchronous/stepping motors, model number M092-FD-310, a Superior

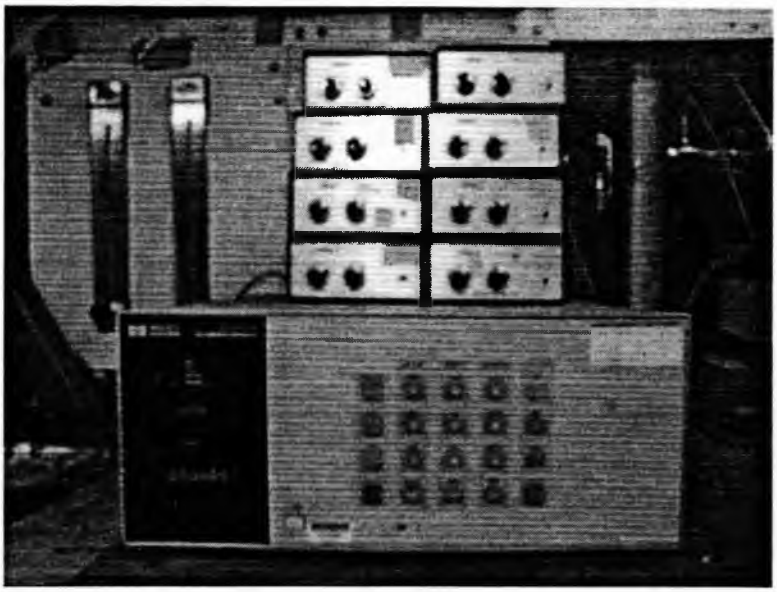

Figure 2.21 Data acquisition system and Carrier demodulators.

Electric SLO-SYN 2000 programmable motion controller model number SS 20001, and a Superior Electric SLO-SYN 2000 drive, model number SS2000DS.

2.2 Safety Features

To ensure that the test facility is safe, during each blow down run, a number of procedures and special apparatus are used. These include pressure relief valves, manual shut off valves, and hearing and eye protection for the operator. Two pressure relief valves are located just after the Fisher regulator that controls the main air supply to the test section. These Kunkle relief valves, model 6010JHV01-KM, have a set vent pressure of 414 kPa (60 psig) and open if the pressure down stream of the Fisher regulator exceeds 414 kPa. Figure 2.23 shows the Kunkle pressure relief valves. A manual shutoff valve and a flow regulating valve, seen in Figures 2.24 and 2.25, respectively, offer additional safety protection. These are also located between the Fisher regulator and the heater

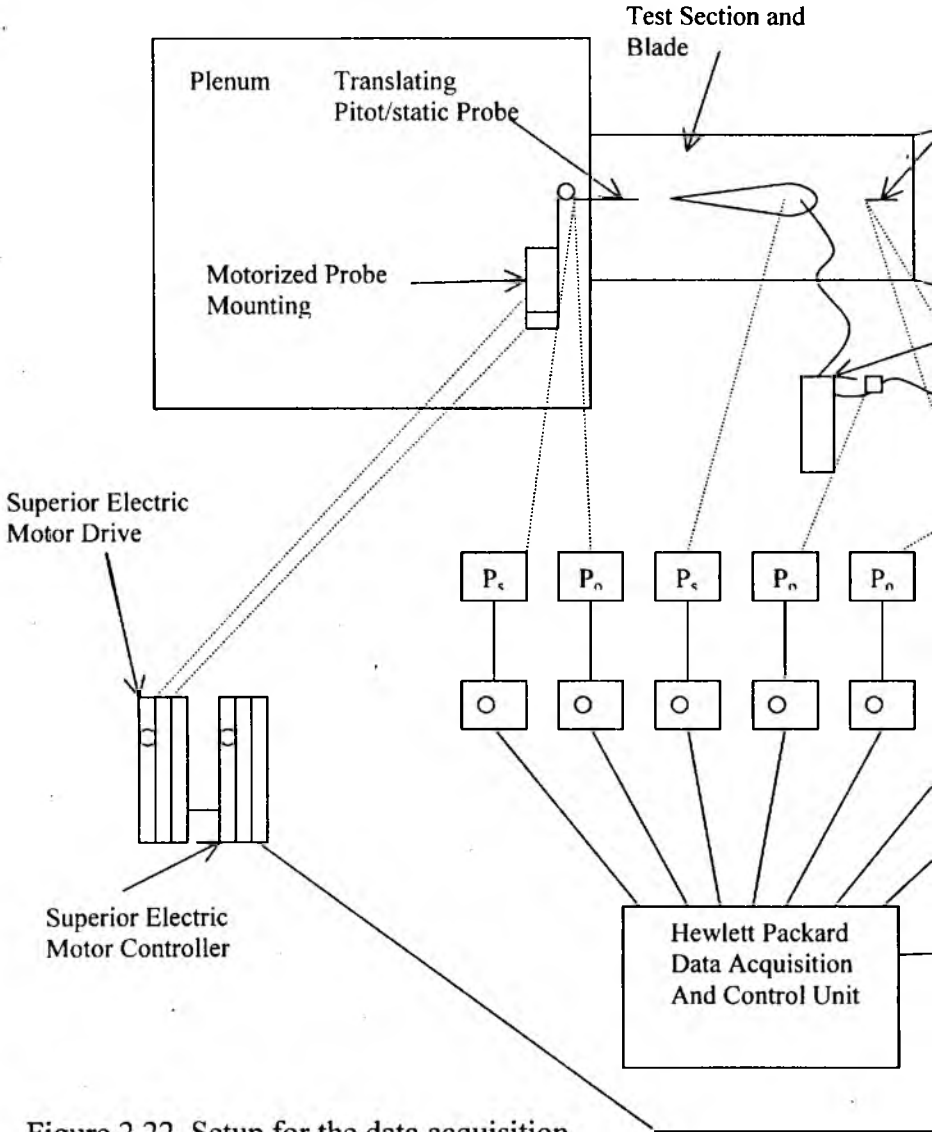

Figure 2.22 Setup for the data acquisition

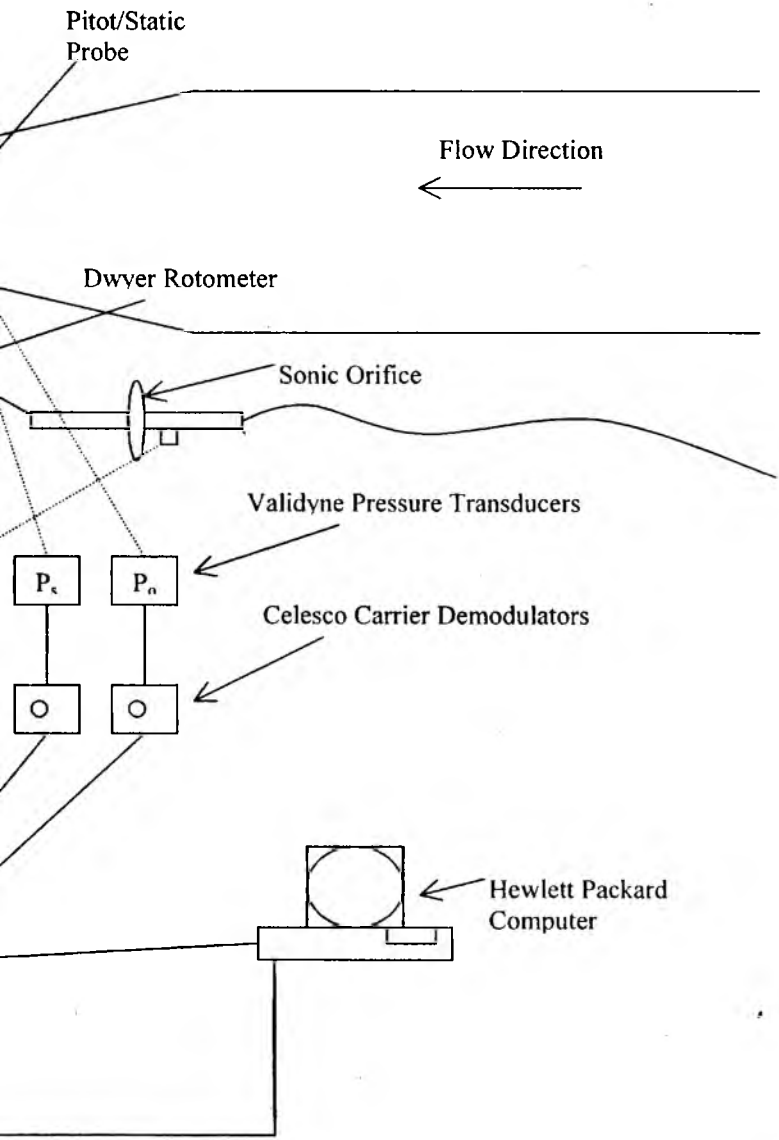
Pitot/Static
Probe
Flow Direction
Dwyer Rotometer
Sonic Orifice
Validyne Pressure Transducers
Celesco Carrier Demodulators
Hewlett Packard
Computer

Figure 2.23 Kunkle relief valves.

tank. The manual shutoff valve is a Centerline 51, operated with a side-mounted hand wheel. The valve has a 50:1 closure ratio. The flow regulating valve is a 25.4 cm (10 inch) inner diameter Neles Jamesbury Waffer-sphere valve with a type NE726 D/L electro-pneumatic positioner and a series D60S II actuator. A Honeywell electronic controller, model number DC 100270701000, controls this valve and is located on the control panel shown in Figure 2.5. This valve is set at 60% open during blow down runs. If an emergency arises, this valve can be closed by simply shutting off the main power to the system or by operating a switch that is located on the control panel. Every person in the room wears ear and eye protection as the test facility is in operation. Ear and eye protection devices are seen in Figure 2.26.

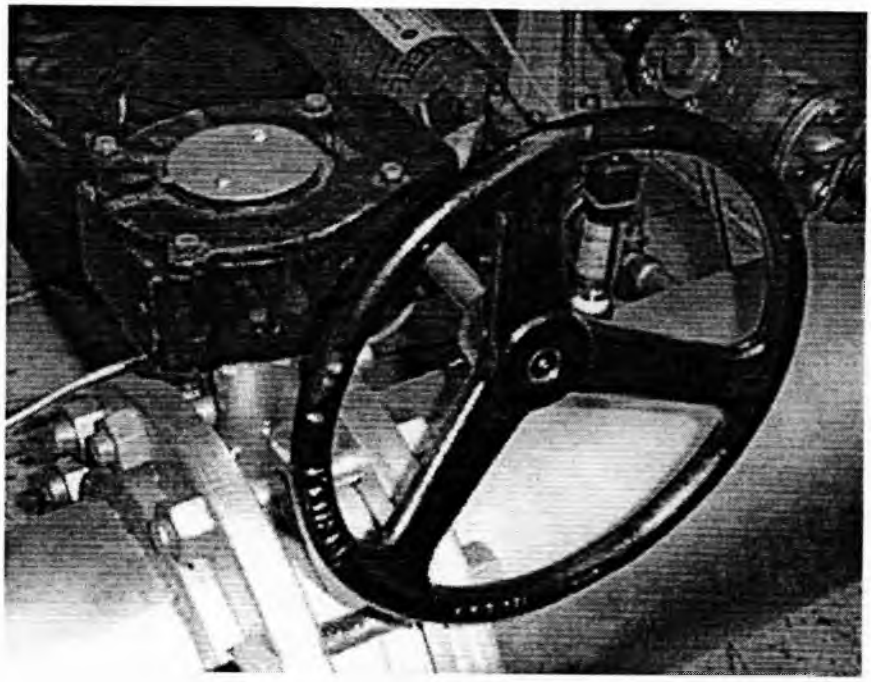

Figure 2.24 Manual shutoff valve.

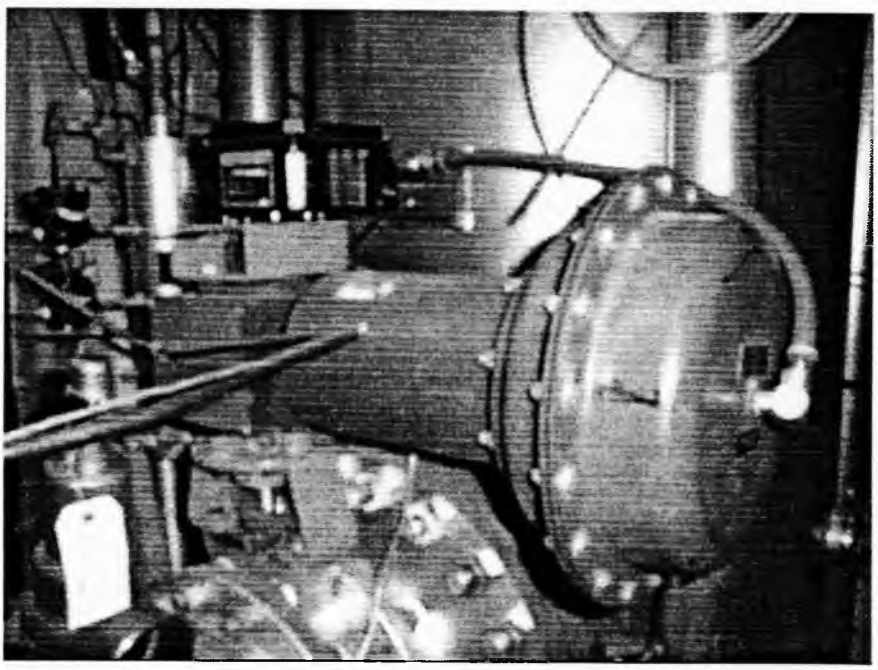

Figure 2.25 Flow regulating valve.

Figure 2.26 Ear and eye protection.

CHAPTER 3

QUALIFICATION OF EXPERIMENTAL APPARATURS AND PROCEDURES

This chapter describes the many different tests that were conducted to qualify the experiment apparatus and procedures.

3.1 Test Section Flow Uniformity

The components of the experiment apparatus, just proceeding the test section, consist of a reducing nozzle and a cylindrical heater tank. The large heater tank is lined with firebrick on the inside. This device acts like a plenum. The reducing nozzle then creates a uniform, steady flow through the test section. Measurements of the total and static pressure readings at different positions at the test section inlet were used to identify the test section uniformity. Total pressure readings were also taken with a stationary probe that was located approximately in the center of the test section inlet. Pressure readings were taken at nine different linear positions. The first and last positions of the linearly moving probe were 5.08 cm (2 inches) above and below the center of the test section inlet respectively, with each of the nine readings 1.2 cm (½ inch) apart. The first and last positions of the probe were 1.2 cm (½ inch) away from the edge of the test section wall.

The readings from these tests are given in Table 3.1. This table also contains readings normalized by dividing each of the pressures by the total pressure taken by the stationary probe, and Mach numbers that were obtained from measurements of the stagnation and static pressures using the following equation

$$M = \sqrt{\left(\left(\frac{P_t}{P_s}\right)^{k-1/k} - 1\right)\frac{2}{k-1}} \qquad (3.1)$$

Figure 3.1 shows the inlet pressures at their respective positions at the test section inlet. The largest difference seen between any position is at 0 to 1.27 cm (0 to 0.5 inch) above the center of the test section where the difference is only 1.24 kPa (0.18 psia). Figure 3.2 shows normalized pressures with a difference of less than 0.0002 between any inlet positions. The small variations are due to small differences between run conditions. Figure 3.3 shows the variation of the Mach number at the test section inlet with differences between positions less than 0.003 Mach number units. From Table 3.1 and Figures 3.1, 3.2, and 3.3, the test section inlet has very uniform flow. There are two yaw

Table 3.1 Results from inlet graphing tests.

Position	P_{ls}	P_{lt}	P_{ht}	M_l	Position	P_{lsn}	P_{ltn}	P_{htn}
cm	kPa	kPa	kPa	kPa	cm	-	-	-
5.08	188.56	195.95	195.86	0.2346	5.08	0.9627	1.0005	1
3.81	189.00	196.40	196.35	0.2346	3.81	0.9625	1.0003	1
2.54	188.45	195.85	195.62	0.2350	2.54	0.9633	1.0011	1
1.27	188.13	195.58	195.38	0.2360	1.27	0.9629	1.0010	1
0	189.14	196.71	196.60	0.2372	0	0.9621	1.0006	1
-1.27	188.45	195.93	195.81	0.2363	-1.27	0.9623	1.0006	1
-2.54	188.44	195.90	195.80	0.2360	-2.54	0.9624	1.0005	1
-3.81	188.32	195.81	195.69	0.2364	-3.81	0.9624	1.0006	1
-5.08	187.43	195.86	195.82	0.2368	-5.08	0.9619	1.0002	1

pressure ports on the exit pitot-static probe. Figure 3.4 shows the pressures taken at these ports. This figure shows that the probe is parallel to the main airflow of the test section within 2°.

3.2 Test Section Flow Variation With Time

For all tests performed on the University of Utah Transonic Wind Tunnel prior to December 4 1998, pneumatic controls were used to control the main regulator that controlled the pressure and volume flow rate of air in the facility. The pneumatic controls worked fairly well but did not give the level of steadiness desired. In order to resolve this problem, an electronic controller for the regulator replaced the pneumatic controller. This electronic controller is faster and more accurate than the pneumatic controller and is much easier to adjust. Numerous runs were performed to find the best setting for the electronic controller.

Figure 3.5 shows the inlet total and static pressure variations with time as the pressure regulator is operated using pneumatic controls. The pressure oscillates approximately 5.17 kPa (¾ psi) and decays approximately 6.89 kPa (1 psi) in 15 seconds. Figure 3.6 shows the total and static pressure variations with time using the electronic controller. The oscillation in the pressure is very close to that of the pneumatic controller but the pressure remains steady at 193.05 kPa (28 psi) for up to 45 to 50 seconds. The best setting for the electronic controller is 296.5 kPa (43 psig) for the set point, 85% for the proportional setting, and 150% for the integral setting. Figure 3.7 shows the repeatability of the settings. Figure 3.8 shows that if the settings are changed to 310 kPa (45 psig) for the set point, 90% for the proportional setting, and 150% for the integral setting, there is no change in the how the regulator operates. If just the proportional band

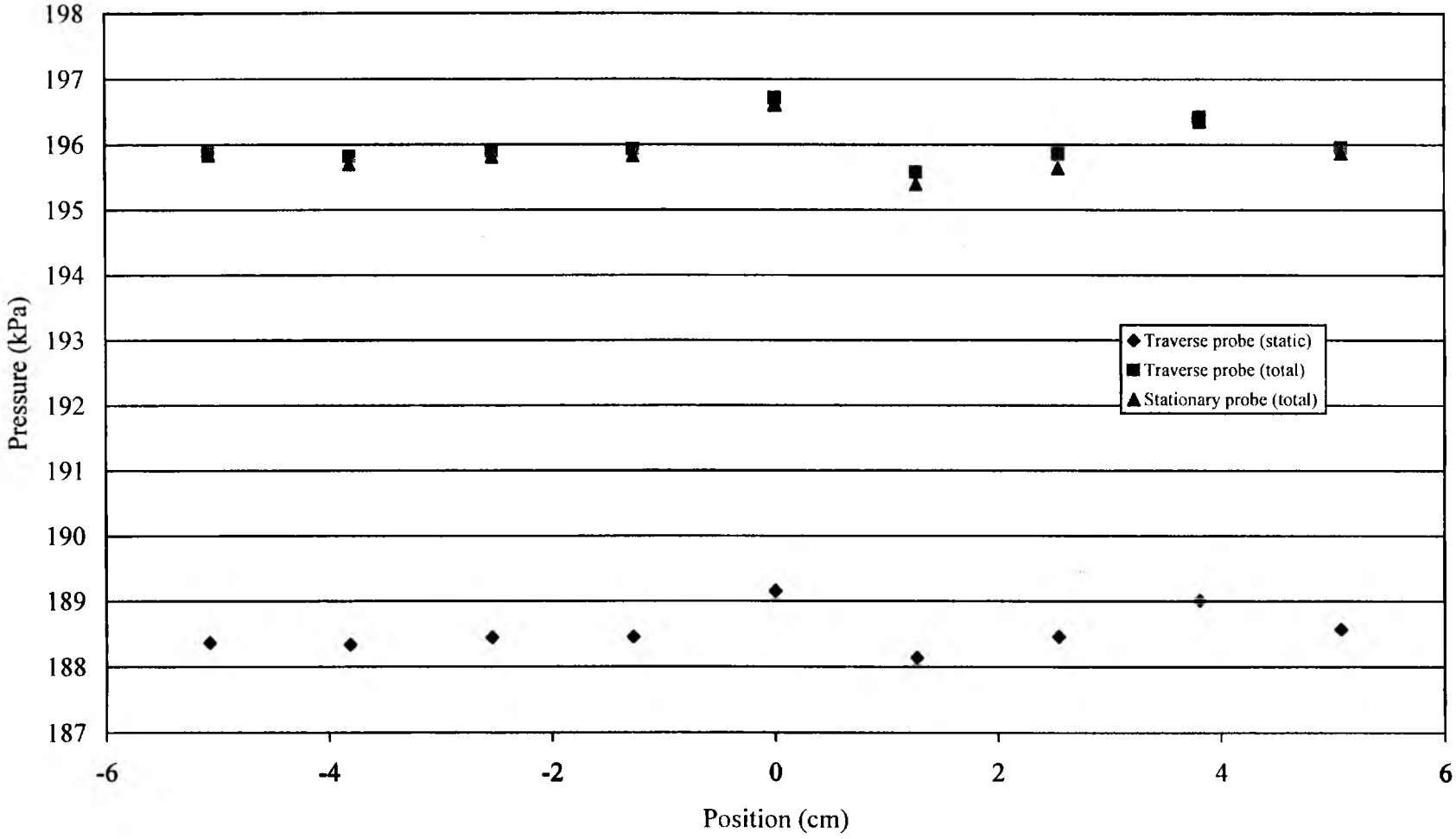

Figure 3.1 Inlet pressure profile.

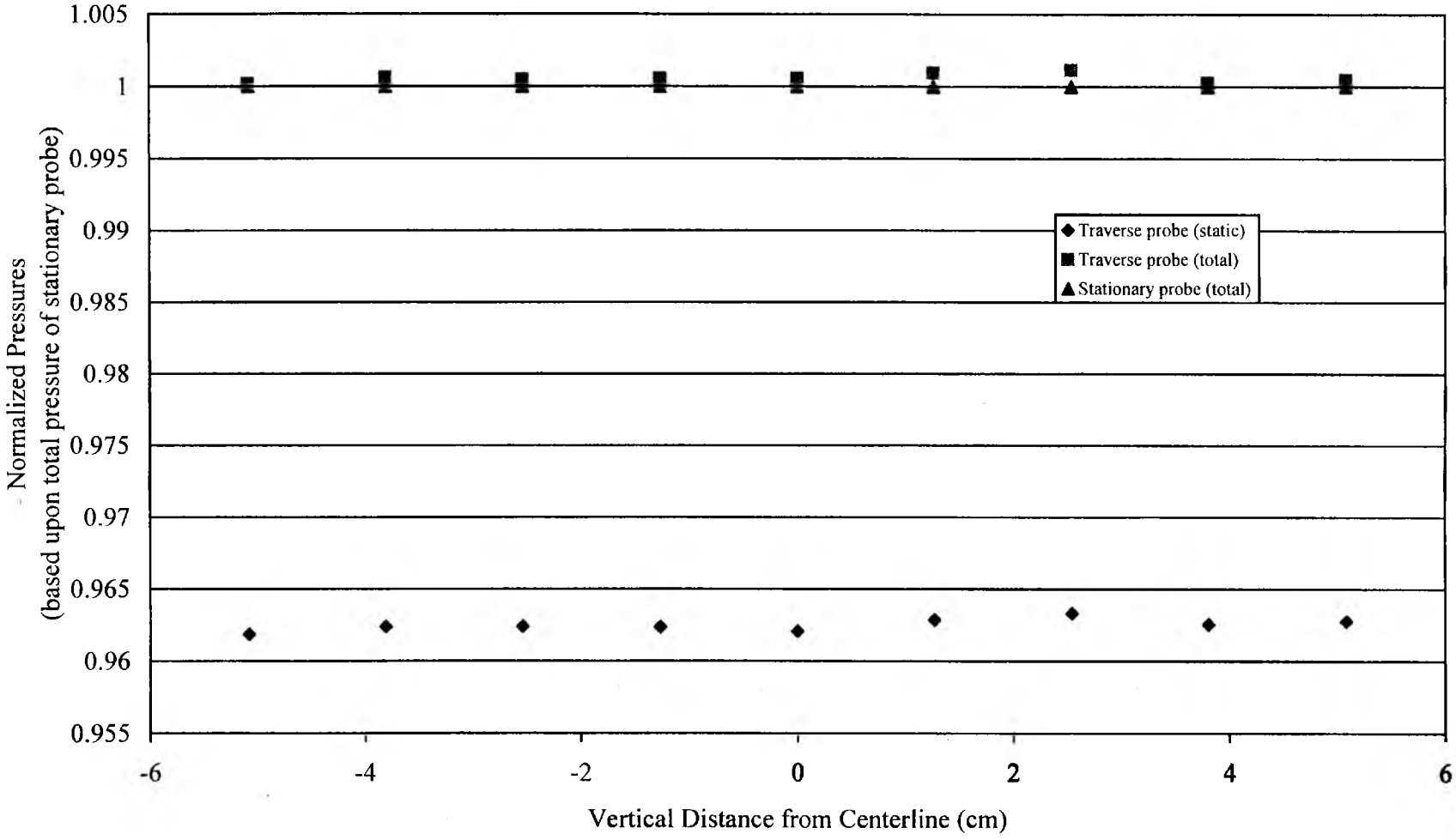

Figure 3.2 Normalized inlet pressure profile.

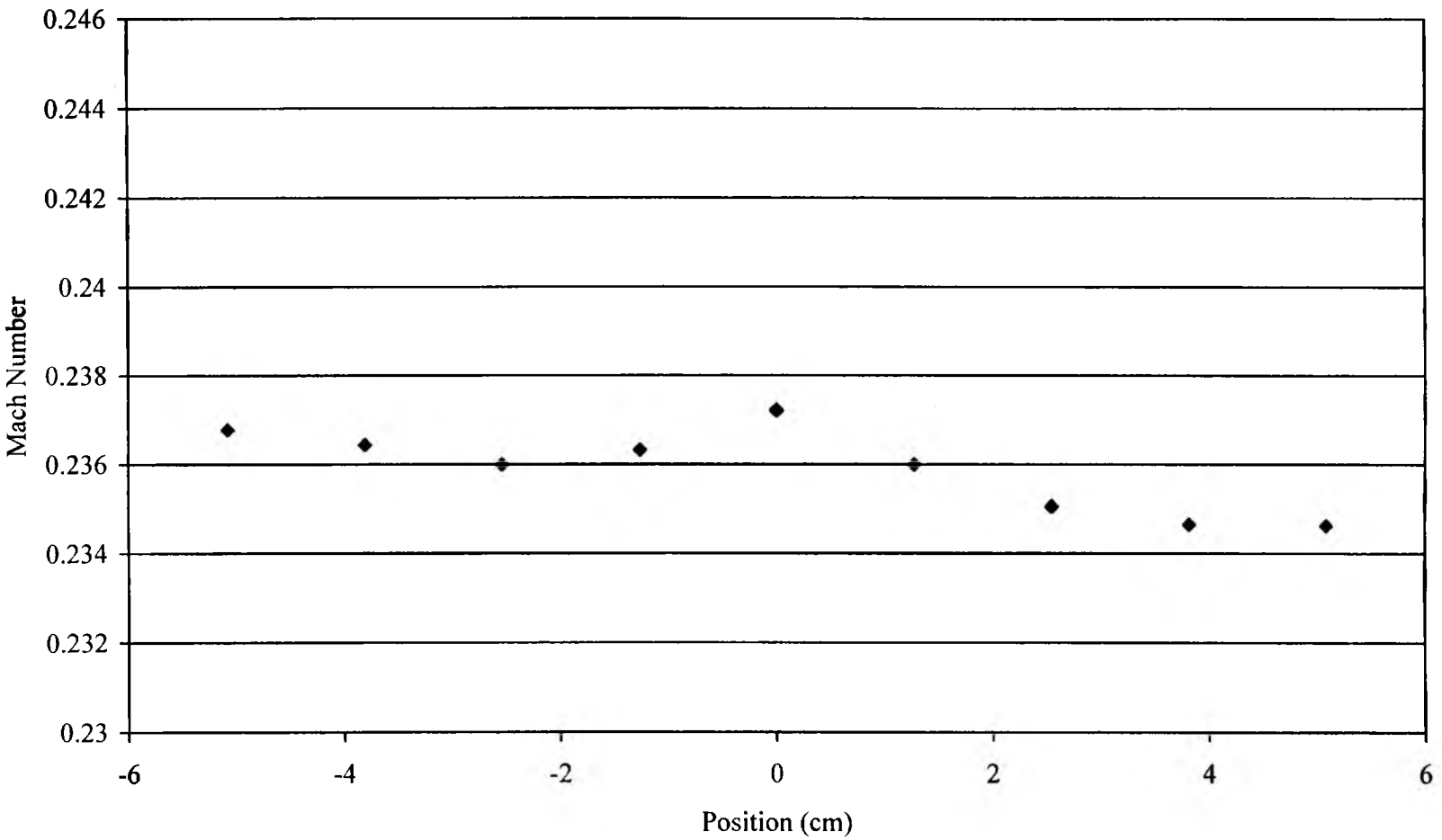

Figure 3.3 Mach number inlet profile.

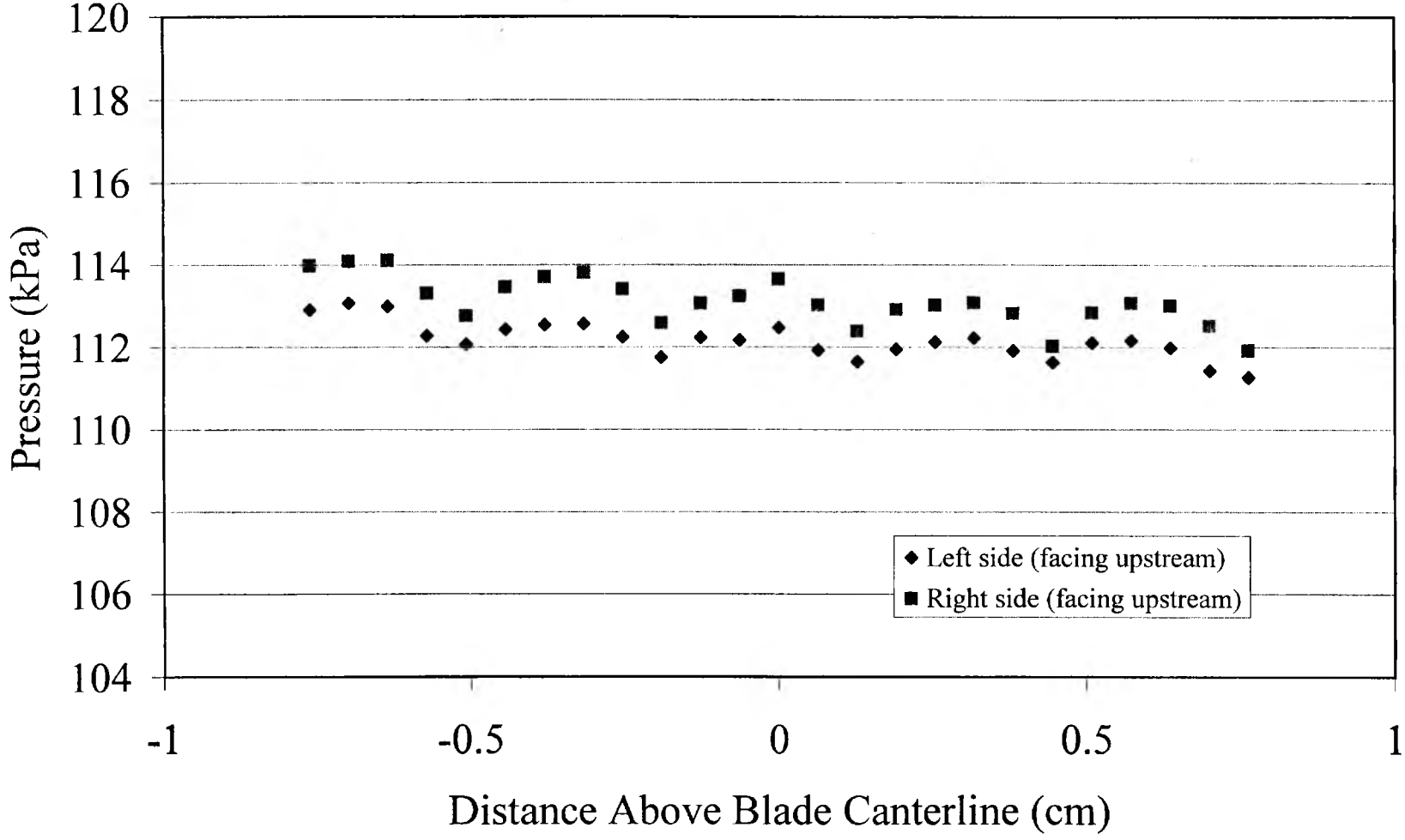

Figure 3.4 Comparison of static pressure on the left and right sides of the exit pitot tube.

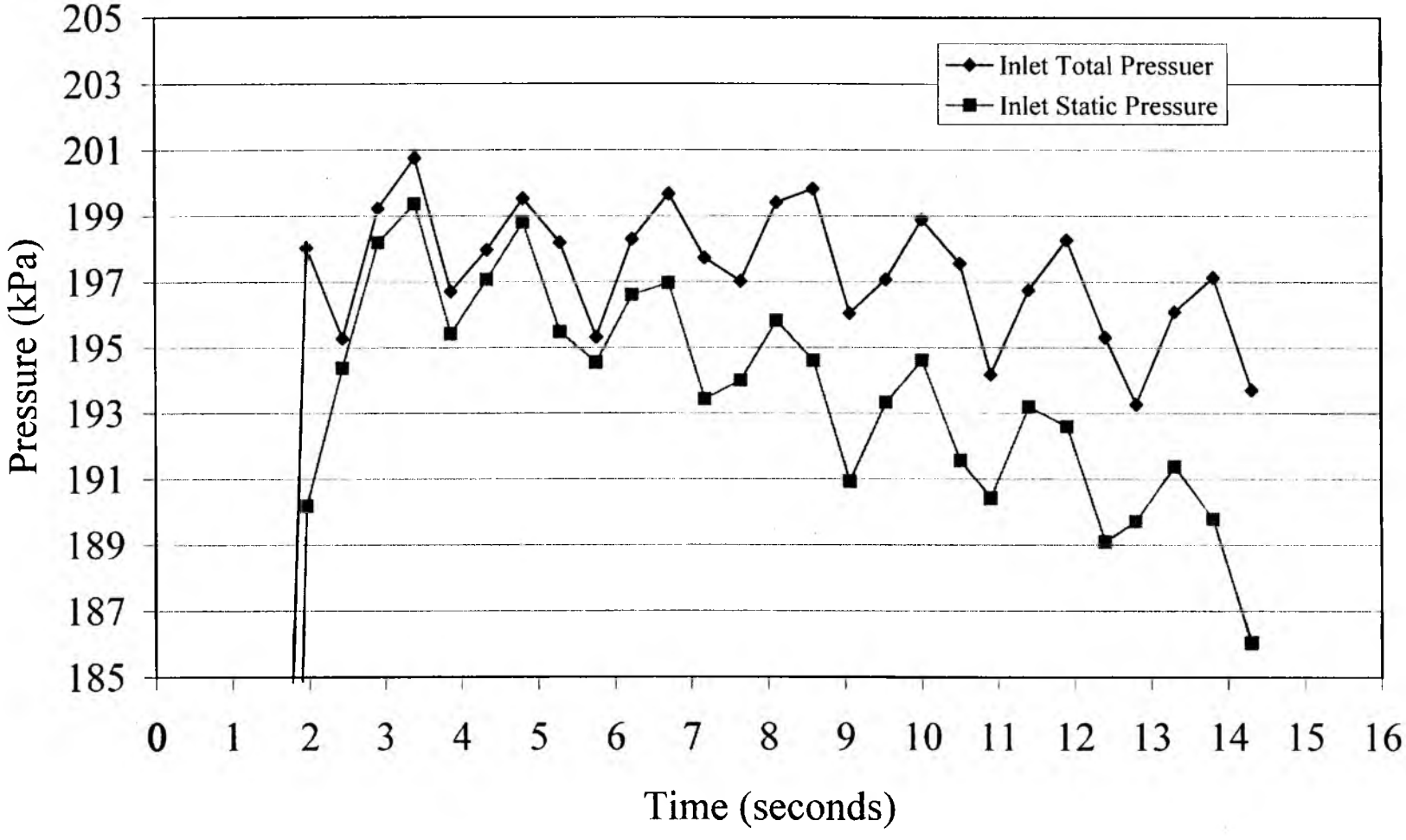

Figure 3.5 Inlet pressure variation with time (pneumatic controls).

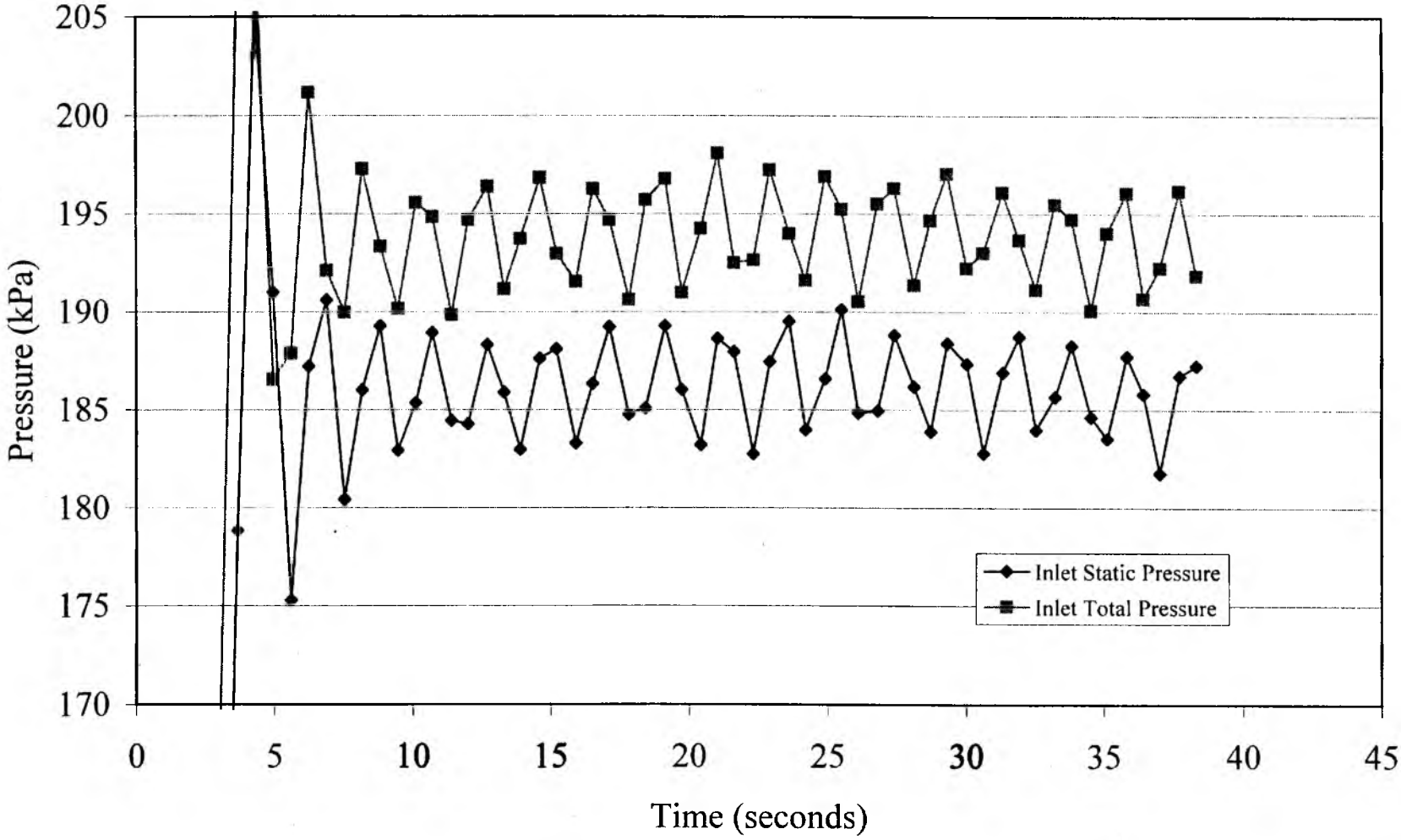

Figure 3.6 Inlet pressure variation with time (electronic controls).
Settings: Proportional 85% Intergral 150% Set Pressure 43 psi.

was set higher, the oscillation in the pressures would become 3.45 kPa (½ psi) instead of 5.17 kPa (¾ psi), but the inlet pressure would drop to approximately 158.58 kPa (23 psi). In order to compensate for the drop in pressure, the set pressure would have to be 310.26 kPa (45 psig) instead of 296.50 kPa (43 psig). This higher pressure produces oscillations that are approximately 5.17 kPa (¾ psi), the same as the lower setting of 296.50 kPa (43 psig). Figure 3.9 shows the maximum duration of a test. It is seen that from approximately 5 seconds to 50 seconds the inlet pressure is approximately constant. Thus testing time durations are around 45 seconds.

3.3 Test Section Flow Structure From Schlieren Imaging

Density variations in air within a shock wave can be seen using Schlieren imaging. A Schlieren image is obtained by reflecting light off of mirrors and through the test section. Figure 3.10 shows a sequence of Schlieren images. The probe can be seen at the right side of the images as a dark horizontal line, and the trailing edge of the blade is on the left side of the images. The flow is traveling from the left to the right in these images. The probe is 5.71 cm (2.25 inches) down stream from the trailing edge of the test blade. This is 0.75 of a chord length down stream.

The top image has no cross flow, so it therefore has no shock wave. The next four images have air flowing across them and a pair of trailing edge shock waves are seen. From these results, it is evident that: (i) no shock waves form in front of the probe, (ii) the trailing edge shock waves do not reflect off the top or bottom walls of the test section, (iii) the probe does not affect the trailing edge shock wave at any position it is placed, and (iv) the trailing edge shock wave remains in place for the duration of the test, which means that steady flow conditions exist for the entire test sequence.

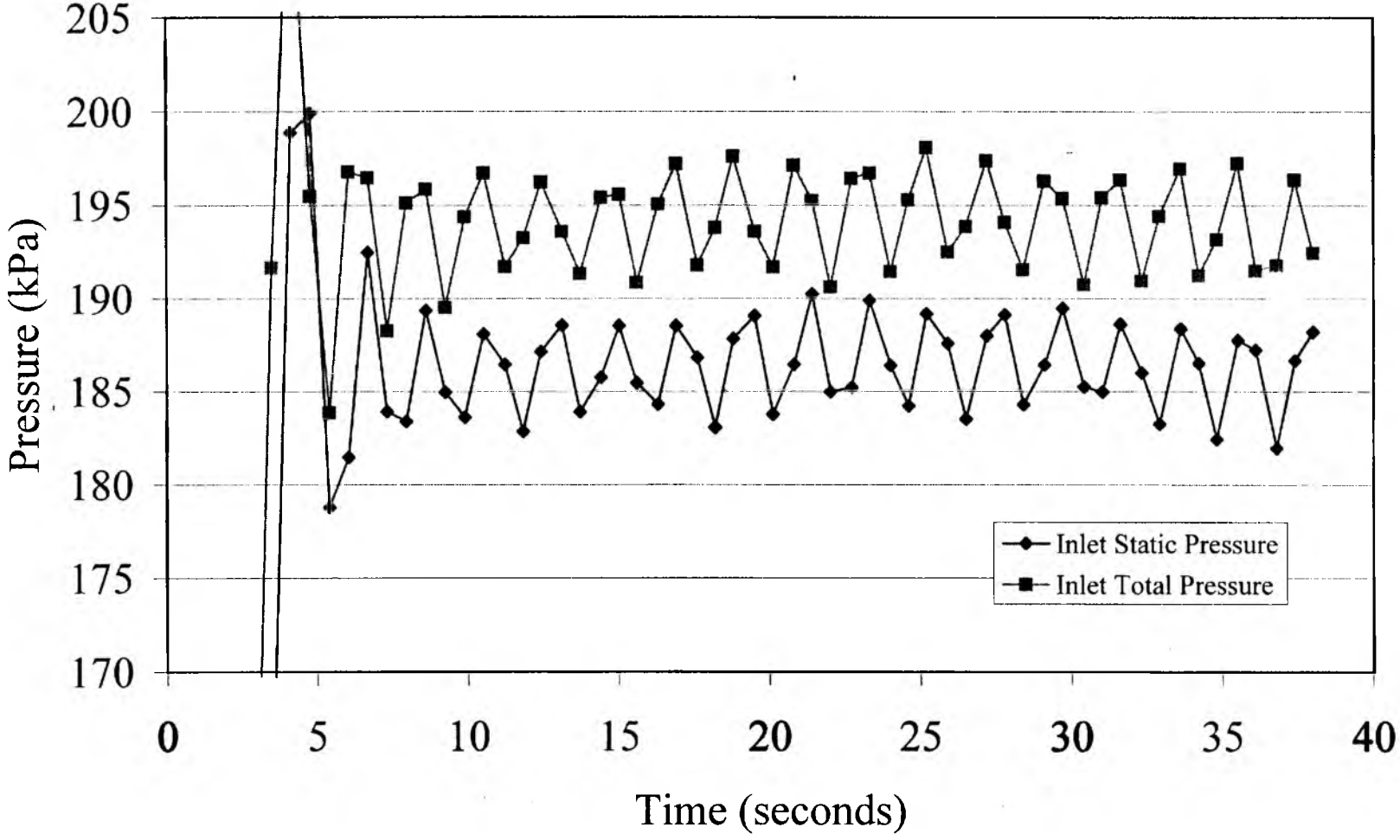

Figure 3.7 Inlet pressure variation with time (electronic controls).
Settings: Proportional 85% Integral 150% Set Pressure 43 psi.

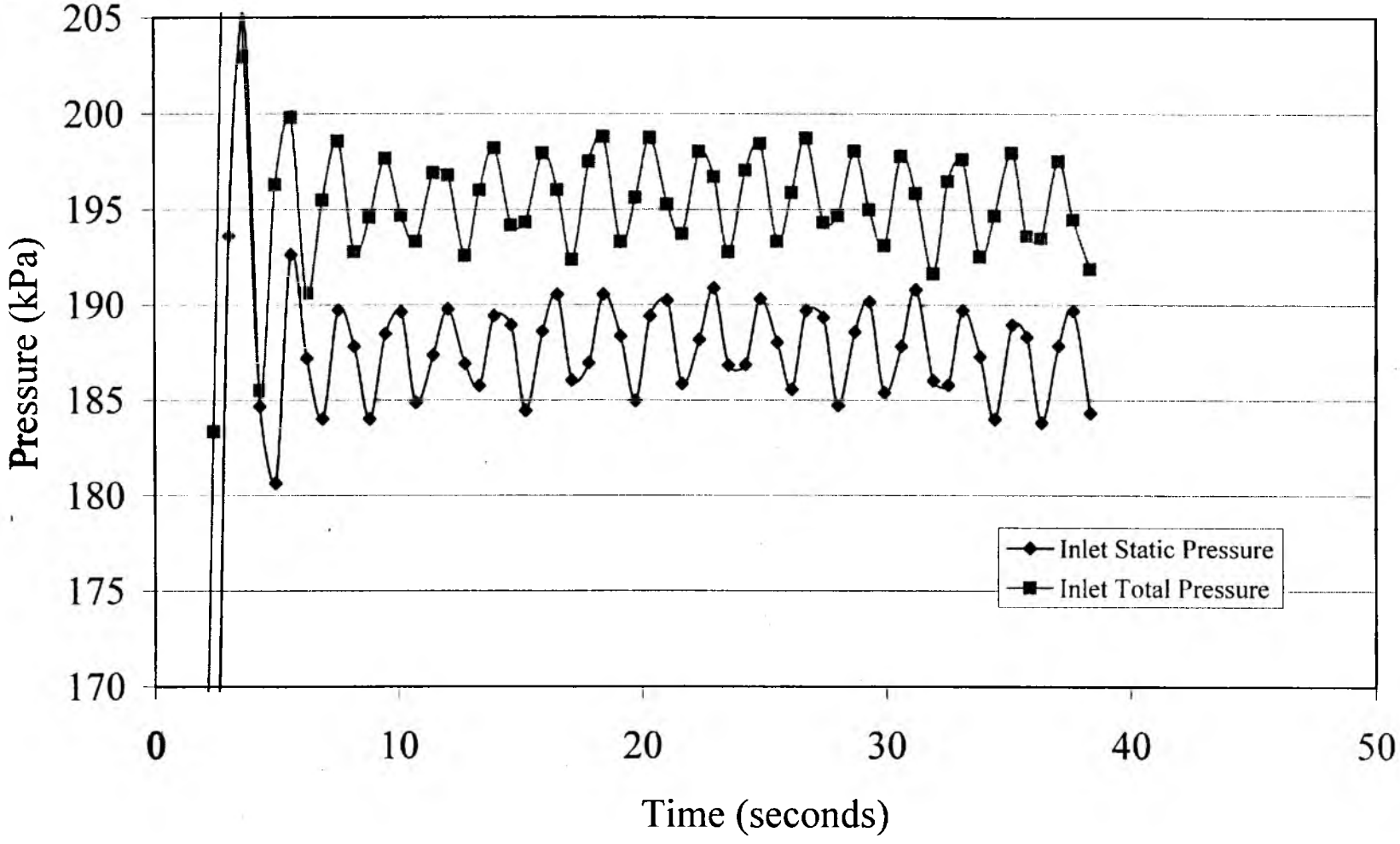

Figure 3.8 Inlet pressure varriation with time (electronic controls).
Settings: Proportional 90% Integral 150% Set Pressure 45 psi.

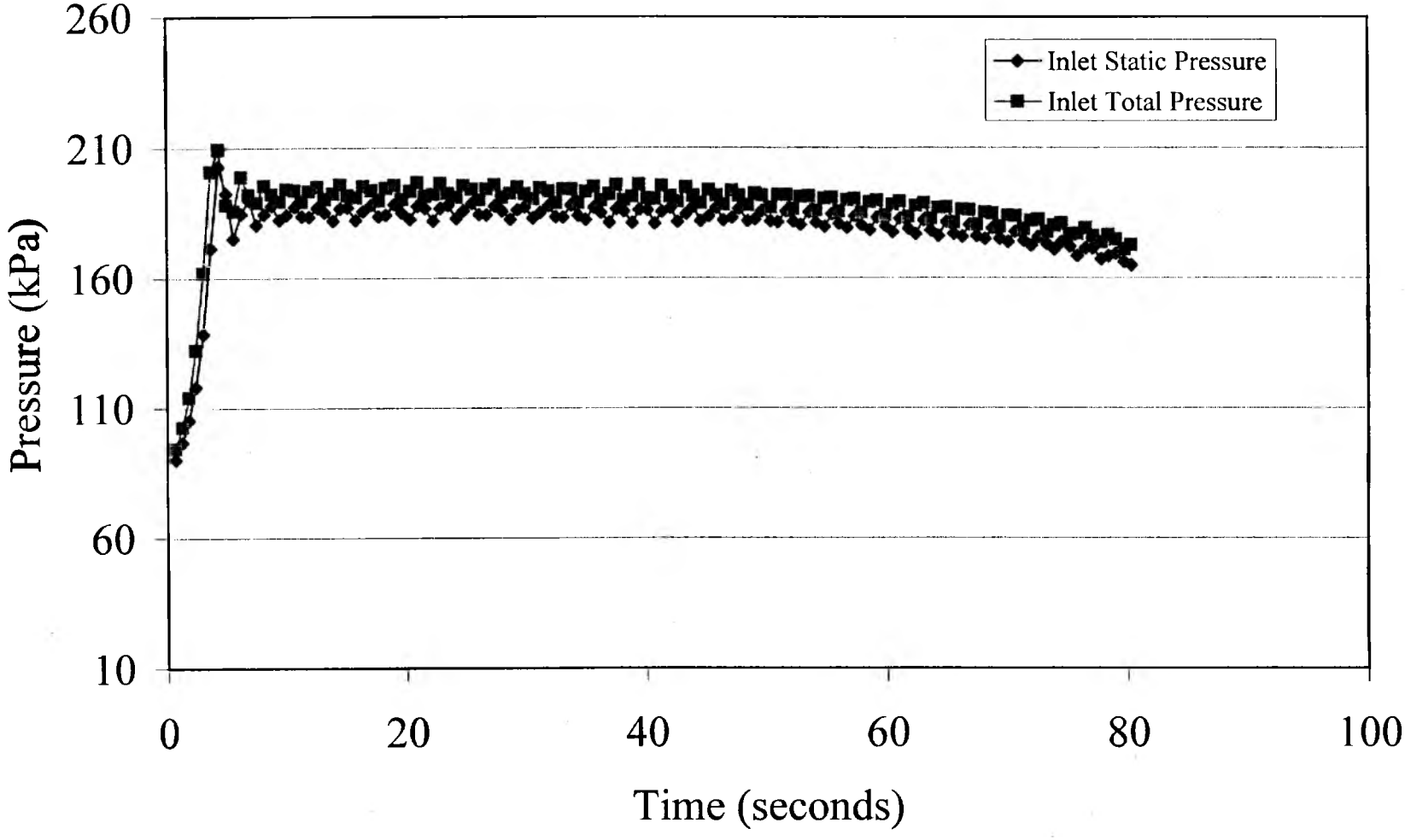

Figure 3.9 Pressure variation with time during typical blowdown test.

Position 1 With No Trailing Edge Shock Wave

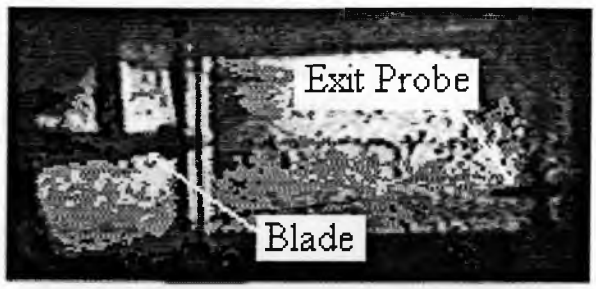

Position 1 With Trailing Edge Shock Wave

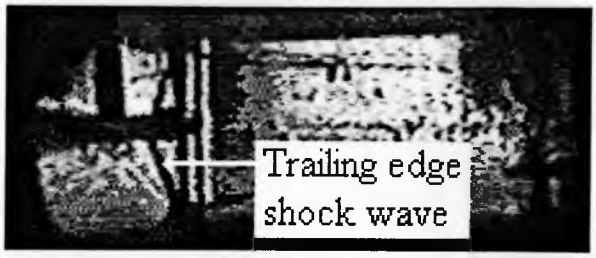

Position 2 With Trailing Edge Shock Wave

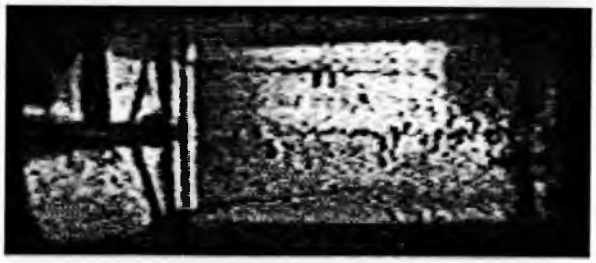

Position 3 With Trailing Edge Shock Wave

Position 4 With Trailing Edge Shock Wave

Figure 3.10 Schlerien images (transonic flow across a turbine blade)

3.4 Mach Number and Pressure Distribution Around Test Blade

To match engine operating conditions along the suction surface of a rotor blade located in the first stage of a transonic turbine, especially constructed contoured top and bottom walls and blade profile were used, which were produced by Pratt and Whitney. These provide the appropriate pressure gradients and proper Mach number distributions along the blade surfaces. Figure 3.11 shows a blade with pressure taps. Table 3.2 shows the locations of the holes in the pressure tap blade. Figure 3.12 shows a schematic of the blade with pressure tap locations. Figure 3.13 shows the Mach number on the top and on the bottom of the blade as it depends upon the axial location on the blade. This figure also shows the desired distribution from Pratt and Whitney for an operating blade. This figure shows that both the top and the bottom of the blade Mach numbers match the Pratt and Whitney distribution within 2%.

3.5 Film Cooling Flow Injection System

Two systems are used to measure the injectant mass flow rate. With the first, the mass flow rate is measured using a Dwyer flow meter. The Dwyer flow meter reads volumetric flow rates and is multiplied by the density to determine the mass flow rate. The initial volumetric flow rate reading has to be adjusted to account for different atmospheric conditions. The flow rate is first corrected to standard conditions using the following equation

$$\dot{V}_{corrected} = \dot{V}_{Dwyer}\sqrt{\frac{P_{atmospheric} + P_{exit}}{P_{atmospheric}}}\frac{1}{\sqrt{S.G.}} \tag{3.2}$$

Figure 3.11 Pressure tap blade.

Table 3.2 Locations of holes in pressure tap blade.

Point	Hole Center	Hole Center	Surface Location	Surface Location	Diameter
	X	Y	X	Y	
	cm	cm	cm	cm	cm
1	0.428	0.174	0.381	0.292	0.107
2	1.541	0.296	1.524	0.549	0.165
3	2.655	0.307	2.667	0.561	0.165
4	3.783	0.205	3.810	0.458	0.165
5	4.545	0.125	4.572	0.377	0.165
6	5.307	0.045	5.334	0.297	0.165
7	6.083	0.091	6.096	0.217	0.107
8	6.854	0.011	6.858	0.137	0.107
11	0.428	-0.174	0.381	-0.292	0.107
14	3.783	-0.205	3.810	-0.458	0.165
17	6.083	-0.091	6.096	-0.217	0.107

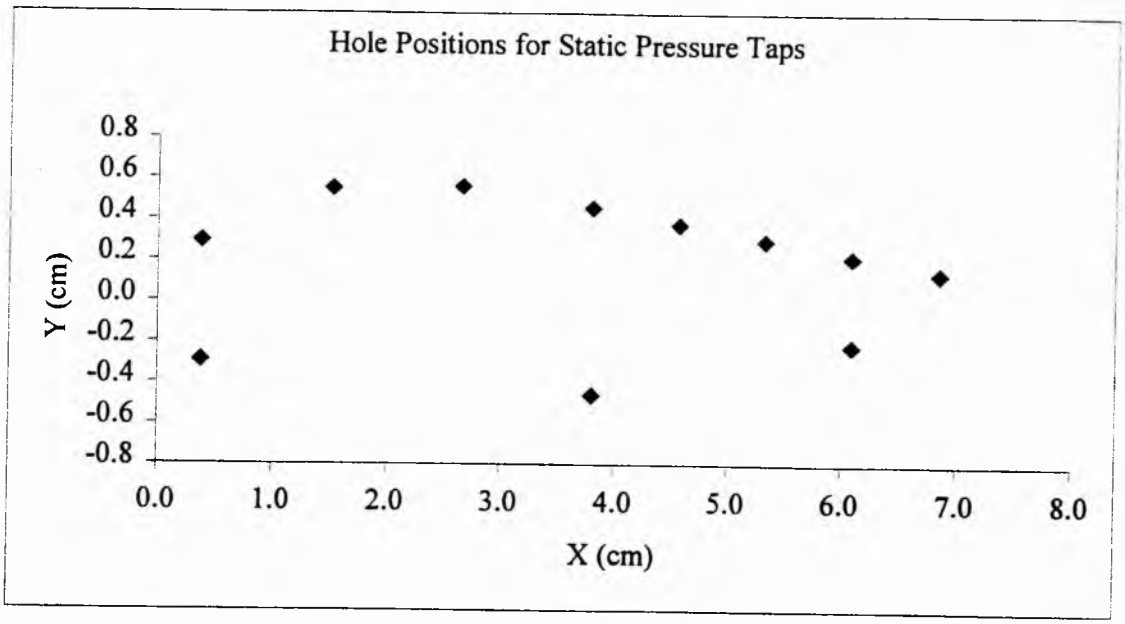

Figure 3.12 Pressure tap blade schematic.

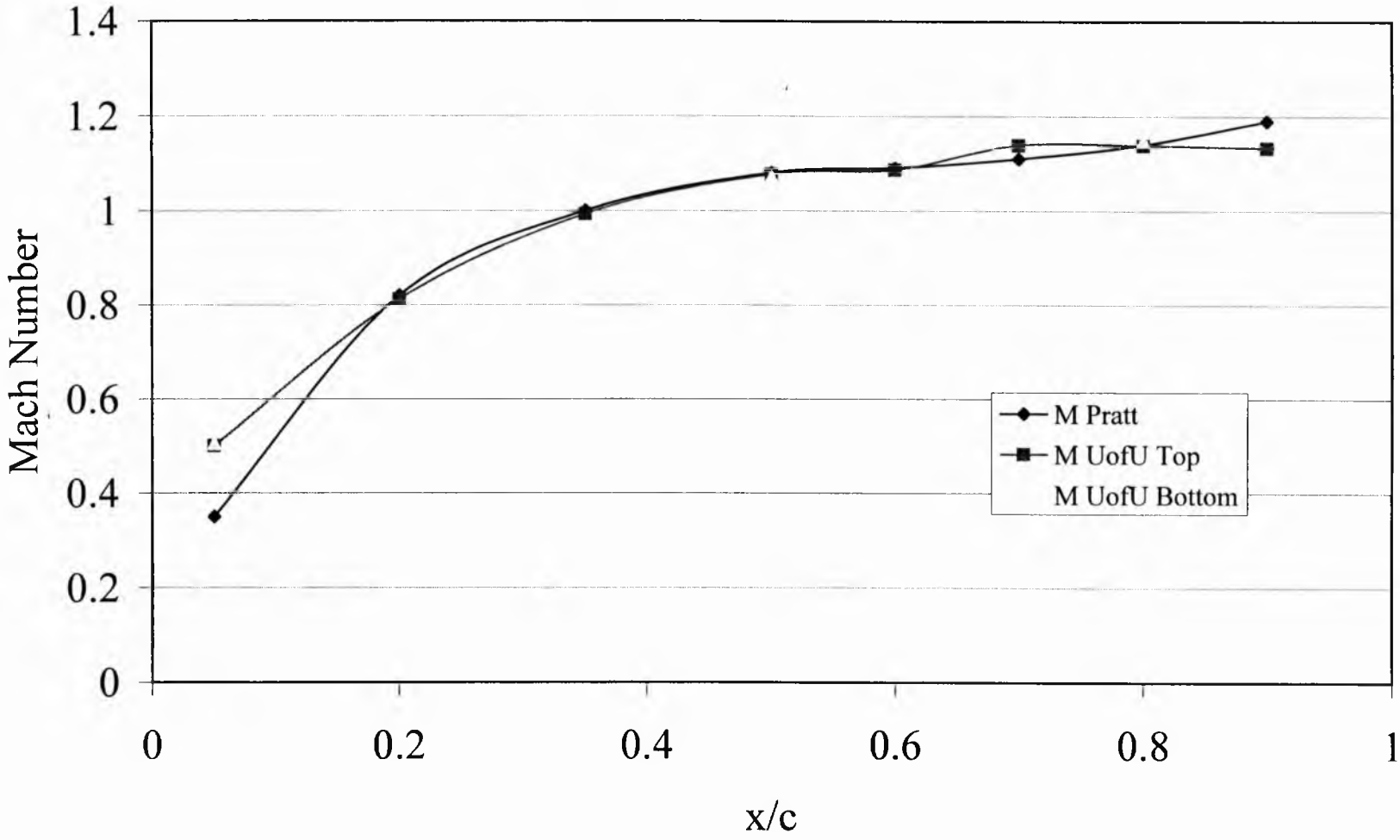

Figure 3.13 Mach number versus axial location.

The corrected volumetric flow rate is then converted to actual conditions from standard conditions using an equation of the form

$$\dot{V}_{actual} = \dot{V}_{corrected} \left(\frac{P_{standard}}{P_{actual}} \right) \left(\frac{T_{actual} + 273}{T_{standard} + 273} \right) \tag{3.3}$$

The last correction factor that is used to match the Dwyer readings to the other mass measuring devices the following correlation is used

$$\dot{V}_{Dwyer} = 0.9293 * \dot{V}_{measurd} - 1.7072 \tag{3.4}$$

The second method to measure the injectant mass flow rate employs a sonic orifice plate. Fleigler's formula is then used for this purpose. To do this, the temperature and pressure just upstream of the orifice are measured. The mass flow rate is then given by

$$\dot{m}_{inj} = \frac{0.532 * A * P_{t,c} * 144}{\sqrt{T_{t,c}}} \tag{3.5}$$

equation 3.5 is derived based on English units.

A check on these measurements was made using a calibrated dry gas meter. Figure 3.14 shows the comparison of the results obtained using all three methods. The three methods agree to with in 1%. The range of volumetric flow rates that can be measured accurately is from 2.55 m^3/hr (90 SCFH (standard cubic feet per hour)) to 8.5 m^3/hr (300 SCFH).

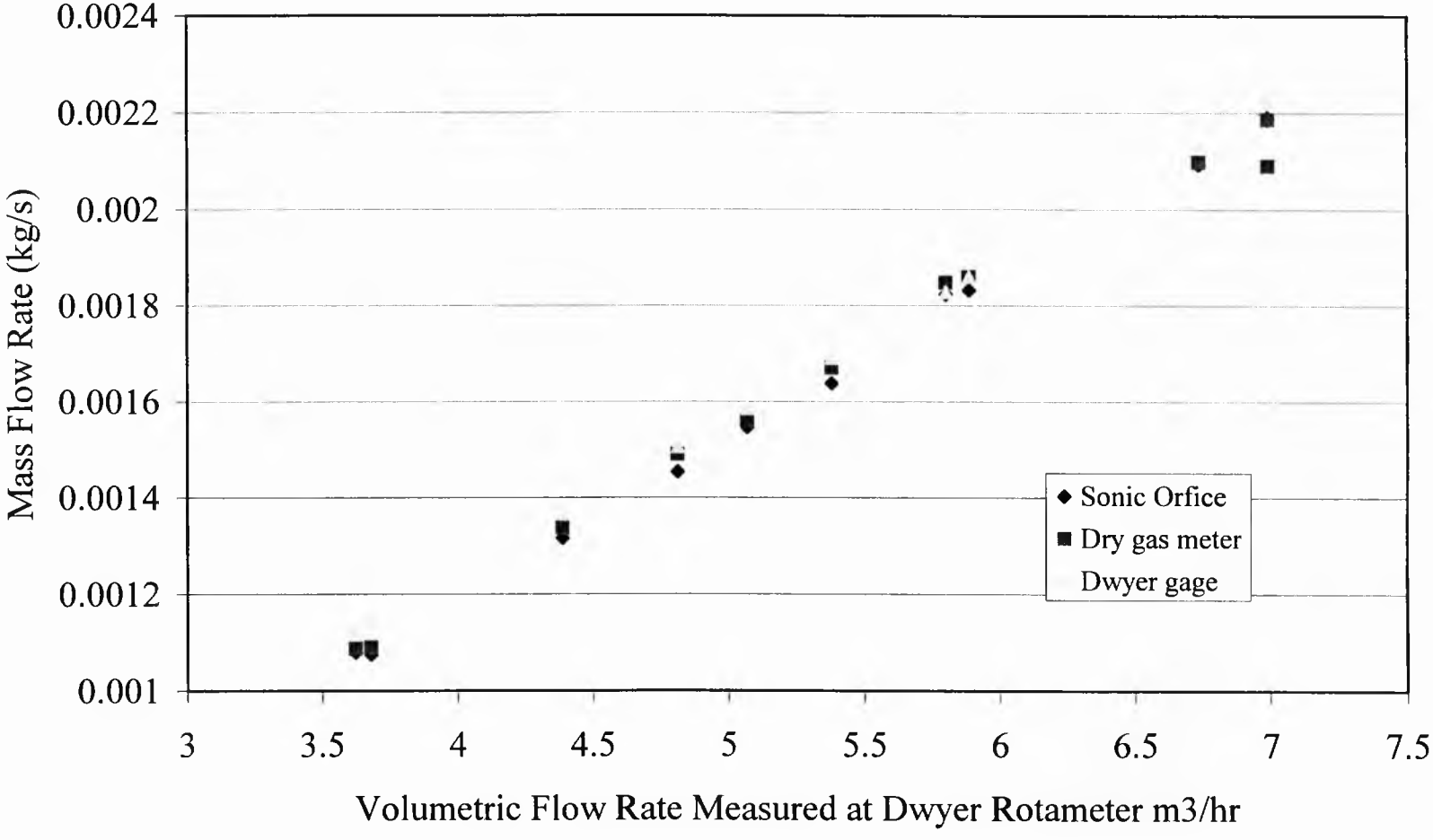

Figure 3.14 Comparison of injectant mass flow rates.

To ensure the mass flow rates that are calculated are correct there must be no leaks in the film cooling air system. To check for leaks, the film cooling air system is turned on with a low flow rate. A syringe is used to distribute a soap substance around any connections in the system. Bubbles then form where a leak is present. Subsequent testing confirmed that there were no leaks in the system.

The film cooling air must be dried before cooling to very low temperatures to avoid the formation of frost and ice in the injection system. To take out very small particulates, and to dry the air, the injectant passes through a particulate filter, a coalescing filter and a desiccant air dryer. Filters are used in conjunction with the dryer because particulates can carry liquid vapor droplets with them. The dryer contains a silica desiccant. This setup was found to work to temperatures as low as $-170\ ^{0}C$ without any frost forming in the film cooling supply lines.

CHAPTER 4

THEORETICAL CONSICERATIONS

This chapter describes theoretical considerations for the study of wake losses and discharge coefficients. Procedures to determine main flow characteristics are described first, followed by procedures to determine injectant flow characteristics, and procedures to determine discharge coefficients.

4.1 Main Flow Characteristics

Mach numbers at the inlet and exit of the test section are determined from the measured stagnation and static pressures using equations of the form

$$M_{i,\infty} = \sqrt{\left(\left(\frac{P_{ti,\infty}}{P_{si,\infty}} \right)^{k-1/k} - 1 \right) \frac{2}{k-1}} \tag{4.1}$$

and

$$M_{e,\infty} = \sqrt{\left(\left(\frac{P_{te,\infty}}{P_{se,\infty}} \right)^{k-1/k} - 1 \right) \frac{2}{k-1}} \tag{4.2}$$

respectively. Recovery temperatures are measured by thermocouples placed at the test section inlet and exit. The recovery factor α for thermocouples with lead wires oriented parallel to the flow direction is 0.68 (Moffat, 1962). Absolute stagnation temperatures are then determined at the test section inlet and exit using the equations given by

$$T_{ti,\infty} - T_{ri,\infty} = (1-\alpha)\left(\frac{(k-1/2)M_{i,\infty}^2}{1+(k-1/2)M_{i,\infty}^2}\right)T_{ti,\infty} \tag{4.3}$$

and

$$T_{te,\infty} - T_{re,\infty} = (1-\alpha)\left(\frac{(k-1/2)M_{e,\infty}^2}{1+(k-1/2)M_{e,\infty}^2}\right)T_{te,\infty} \tag{4.4}$$

respectively. Absolute inlet and exit static temperatures are then given by

$$T_{si,\infty} = \frac{T_{ri,\infty} - \alpha T_{ti,\infty}}{1-\alpha} \tag{4.5}$$

and

$$T_{se,\infty} = \frac{T_{re,\infty} - \alpha T_{te,\infty}}{1-\alpha} \tag{4.6}$$

respectively. The sonic velocity, streamwise velocity and static density at the test section inlet are subsequently given by

$$C_{i,\infty} = \left(kRT_{si,\infty}\right)^{0.5} \tag{4.7}$$

$$U_{i,\infty} = M_{i,\infty} C_{i,\infty} \tag{4.8}$$

and

$$\rho_{si,\infty} = \frac{P_{si,\infty}}{RT_{si,\infty}} \tag{4.9}$$

At the test section exit, the sonic velocity, streamwise velocity and static density are then of the form

$$C_{e,\infty} = \left(kRT_{se,\infty}\right)^{0.5} \tag{4.10}$$

$$U_{e,\infty} = M_{e,\infty} C_{e,\infty} \tag{4.11}$$

and

$$\rho_{se,\infty} = \frac{P_{se,\infty}}{RT_{se,\infty}} \tag{4.12}$$

The mainstream mass flow rate is determined using

$$\dot{m} = \rho_{si,\infty} U_{i,\infty} A_i \tag{4.13}$$

The Reynolds number based on the blade chord is given by

$$\mathrm{Re}_\infty = \rho_{si,\infty} \frac{U_{i,\infty} c}{\mu_{si,\infty}} \tag{4.14}$$

4.2 Injection Flow Characteristics

At the exit of the film cooling holes, the freestream Mach number (M_∞) is 1.065. The freestream absolute static temperature and freestream static pressure at the exit of the film cooling holes are then determined using

$$T_{s,\infty} = 0.815 T_{ti,\infty} \tag{4.15}$$

and

$$P_{s,\infty} = 0.4892 P_{ti,\infty} \tag{4.16}$$

Freestream sonic velocity, streamwise velocity, and static density at the exit of the film cooling holes are then calculated using equations of the form

$$C_\infty = \left(kRT_{S,\infty}\right)^{0.5} \tag{4.17}$$

$$U_\infty = M_\infty C_\infty \tag{4.18}$$

and

$$\rho_{s,\infty} = \frac{P_{s,\infty}}{RT_{s,\infty}} \tag{4.19}$$

To determine the average injectant velocity at the exit planes of the holes, the measured volumetric flow rate of the film cooling air is divided by the area of the film cooling holes. Two methods are used to determine the injectant volumetric flow rate: (i)sonic orfice and (ii)Dwyer rotameter. The dwyer rotameter measurment details are now described. The volumetric flow rate is determined from the Dwyer rotameter in cubic meters per hour (m^3/hr) (SCFH (standard cubic feet per hour)) using procedures described in section 3.5 of Chapter 3. Assuming steady flow, and constant mass flow rate between the exit planes of the holes and the location where the volumetric film flow rate is measured, the volumetric flow rate at the exits of the film cooling holes is given by

$$\dot{V}_c = \frac{\dot{V}_m \rho_m}{\rho_c} = \frac{\dot{V}_o \rho_o}{\rho_c} \tag{4.20}$$

From this equation, one can then obtain

$$\dot{V}_c = \dot{V}_o \left(\frac{P_o}{P_{s,c}} \right) \left(\frac{T_{s,c}}{T_o} \right) \tag{4.21}$$

which is equivalent to

$$\dot{V}_c = \dot{V}_o \left(\frac{P_o}{P_{s,\infty}} \right) \left(\frac{T_{s,c}}{T_o} \right) \tag{4.22}$$

The average velocity at the exit plane of the holes is then of the form

$$U_c = \frac{\dot{V}_c}{A_c} \tag{4.23}$$

The injectant static temperature at the exit planes of the holes is determined using

$$T_{s,c} = \frac{T_{op}}{\left(1 + \left((k-1)/2\right) M_c^2\right)} \tag{4.24}$$

The injectant sonic velocity and injectant Mach number, both at the film hole exits, are then given by

$$C_c = \left(kRT_{s,c}\right)^{0.5} \tag{4.25}$$

and

$$M_c = \frac{U_c}{C_c} \tag{4.26}$$

A second equation used to calculate the injectant Mach number is given by

$$M_c = \sqrt{\left(\left(\frac{P_{t,c}}{P_{s,\infty}} \right)^{k-1/k} - 1 \right) \frac{2}{k-1}}$$

The injectant static density, mass flow rate, and injectant Reynolds number based on hole diameter are then given by

$$\rho_{s,c} = \frac{P_{s,}}{RT_{s,c}} \tag{4.27}$$

$$\dot{m}_c = \rho_{s,c} U_c A_c \tag{4.28}$$

and

$$\mathrm{Re}_c = \frac{\rho_{s,c} U_c d}{\mu_{s,c}} \tag{4.29}$$

respectively.

The following non dimensional film cooling flow parameters are also found. The static temperature ratio is given by $T_{s,c}/T_{s,\infty}$. The static to total temperature ratio is given

by $T_{s,c}/T_{ti,\infty}$. The coolant supply to freestream pressure ratio is given by $P_p/P_{s,\infty}$. The density ratio is given by $\rho_{s,c}/\rho_{s,\infty}$. The velocity ratio is given by U_c/U_∞ . The blowing ratio is given by $\rho_{s,c}U_c/\rho_{s,\infty}U_\infty$. The momentum flux ratio is given by $\rho_{s,c}U_c^2/\rho_{s,\infty}U_\infty^2$. The mass flow rate ratio is given by $2m_c/m$

4.3 Discharge Coefficient Determination

A discharge coefficient is the ratio between the injectant mass flow to the freestream mass flow. A low discharge coefficient means that there are more losses and friction due to passage of film cooling through the holes. Discharge coefficients are found using an equation of the form

$$C_D = \frac{\dot{m}_c}{\dot{m}_{c,ideal}} \tag{4.30}$$

where the injectant mass flow rate is found using the corrected volumetric flow rate and the sonic orifice mass flow rate given by equation (3.5). The ideal mass flow rate of the free stream is found using the following equation

$$\dot{m}_{c,ideal} = A_c P_{o,p} M_c \left(k/RT_{o,p}\right)^{0.5} \left(1+\left((k-1)/2\right)M_c^2\right)^{-(k+1)/2(k-1)} \tag{4.31}$$

The injectant Mach number in this equation is determined using equation (3.1). The static pressure and temperature inside the blade plenum are measured using a wall static pressure tap and a temperature probe placed in the plenum. The cross sectional areas of

the film cooling holes are measured using a high powered microscope and a measuring scale.

CHAPTER 5

EXPERIMENTAL RESULTS

This chapter presents experimental results for Pratt and Whitney Blades 3 and 4 with "ambient" and "cold" film cooling at different blowing ratios. For Blade 3, "ambient" injection corresponds to density ratios from 0.84 to 0.973, and "cold" injection corresponds to density ratios from 1.13 to 1.37. For Blade 4 "ambient" injection corresponds to density ratios from 0.838 to 0.95, and "cold" injection corresponds to density ratios from 1.032 to 1.223.

5.1 Pratt and Whitney Blade 3

Table 5.1 gives the experimental conditions for Blade 3. Included is the volumetric flow rate of the film cooling, density ratios, Mach number ratios, blowing ratios, pressure ratios, and values of integrated aerodynamic loss.

5.1.1 Discharge Coefficients

Blade 3 discharge coefficients for both "ambient" and "cold" film cooling are given in Figures 5.1 and 5.2, which show values for three different pressure ratios for "ambient" and "cold" film cooling with and without freestream cross flow. All baseline data with "no cross flow" are obtained with "ambient" film cooling. "Ambient" film cooling discharge coefficients match baseline data at high pressure ratios but are somewhat lower as the pressure ratios get smaller. "Cold" film cooling discharge

Table 5.1 Experimental conditions, Blade 3.

No Cooling

m3/hr	Density Ratio ρ_c/ρ_∞	Mach Ratio M_c/M_∞	Blowing Ratio m	Pressure Ratio P_{oc}/P_∞	Integral Value of Aerodynamic Losses (N/cm)
0	--	--	--	--	0.650

Ambient Tests

m3/hr	Density Ratio ρ_c/ρ_∞	Mach Ratio M_c/M_∞	Blowing Ratio m	Pressure Ratio P_{oc}/P_∞	Integral Value of Aerodynamic Losses (N/cm)
2.12	0.840	0.460	0.42	1.180	0.671
3.54	0.880	0.700	0.73	1.450	0.795
4.95	0.973	1.010	1.24	2.070	0.893

Cold Tests

m3/hr	Density Ratio ρ_c/ρ_∞	Mach Ratio M_c/M_∞	Blowing Ratio m	Pressure Ratio P_{oc}/P_∞	Integral Value of Aerodynamic Losses (N/cm)
2.69	1.130	0.410	0.47	1.120	0.720
3.54	1.370	0.480	0.65	1.190	0.831
5.38	1.330	0.890	1.28	1.780	0.887

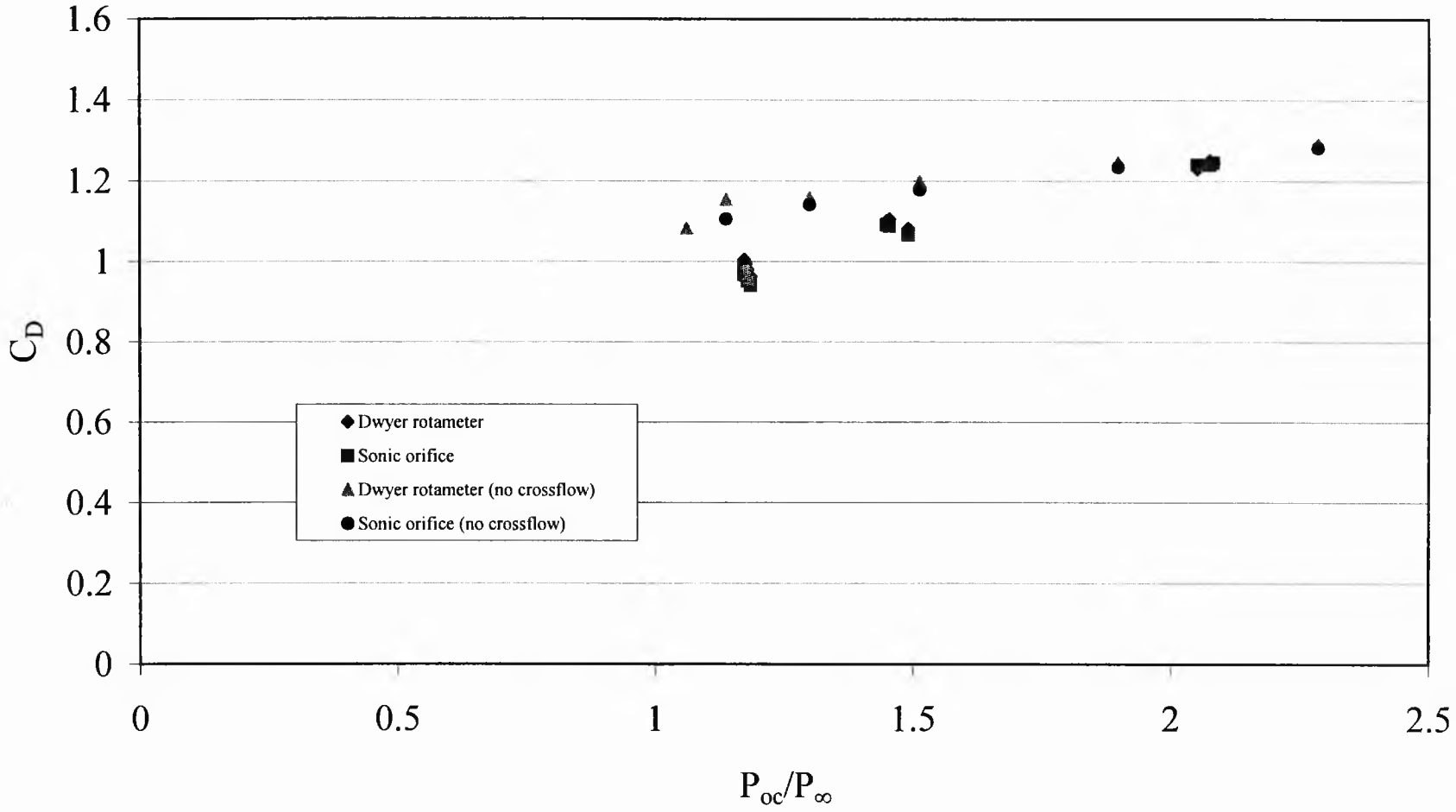

Figure 5.1 Discharge coefficients versus pressure ratios for Blade 3 ("ambient" film cooling).

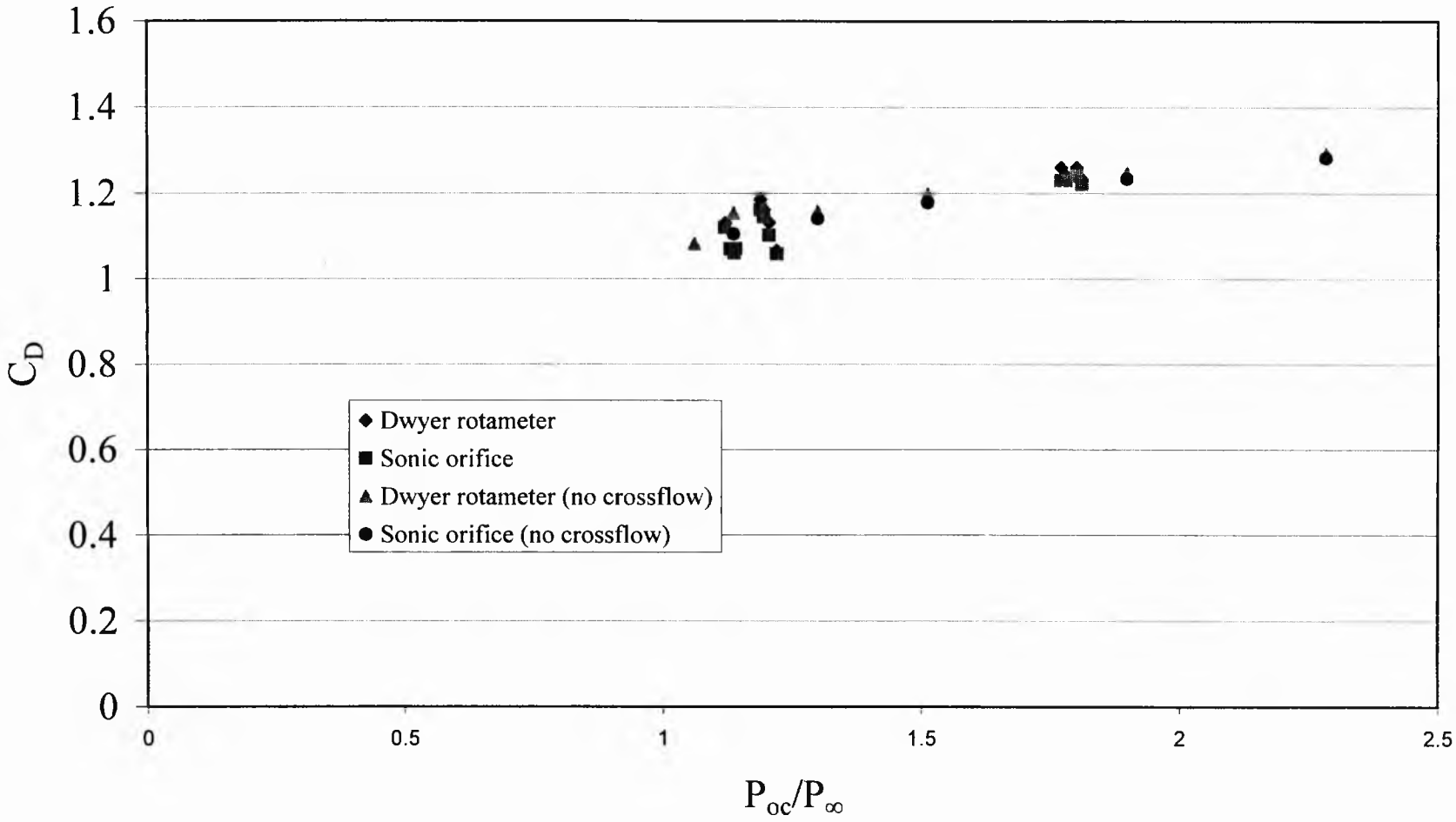

Figure 5.2 Discharge coefficients versus pressure ratios for Blade 3 ("cold" film cooling).

coefficients match the base line for all three blowing ratios. Discharge coefficients shown in these two figures range from 0.94 to 1.3. Some values are greater than one because the hole diameter used for determining discharge coefficients and all other parameters in Table 5.1 (0.381 mm (0.015 in)) is smaller than the actual size.

5.1.2 Wake Characteristics

Plots of the difference between inlet and exit total pressure as dependent upon distance from the airfoil centerline are given in Figures 5.3 to 5.6 for Blade 3. These data provide information on the dependence of aerodynamic losses on film cooling parameters.

Figure 5.3 shows aerodynamic losses with "ambient" film cooling. The greatest losses are measured directly behind the airfoil centerline. Loss magnitudes increase as the mass flow rate of film cooling injectant increases. Figure 5.4 includes contributions from oblique shock waves and "ambient" film cooling. Contributions from the "shock waves" are then removed in Figure 5.3

Figure 5.5 shows aerodynamic losses with "cold" film cooling. Figure 5.6 includes contributions from the oblique trailing edge shock waves. Such contributions are removed from data in Figures 5.3 and 5.5 by subtracting the lowest pressure from all of the pressure values. With this adjustment, freestream pressures are then the same at the test section inlet and exit in Figures 5.3 and 5.5.

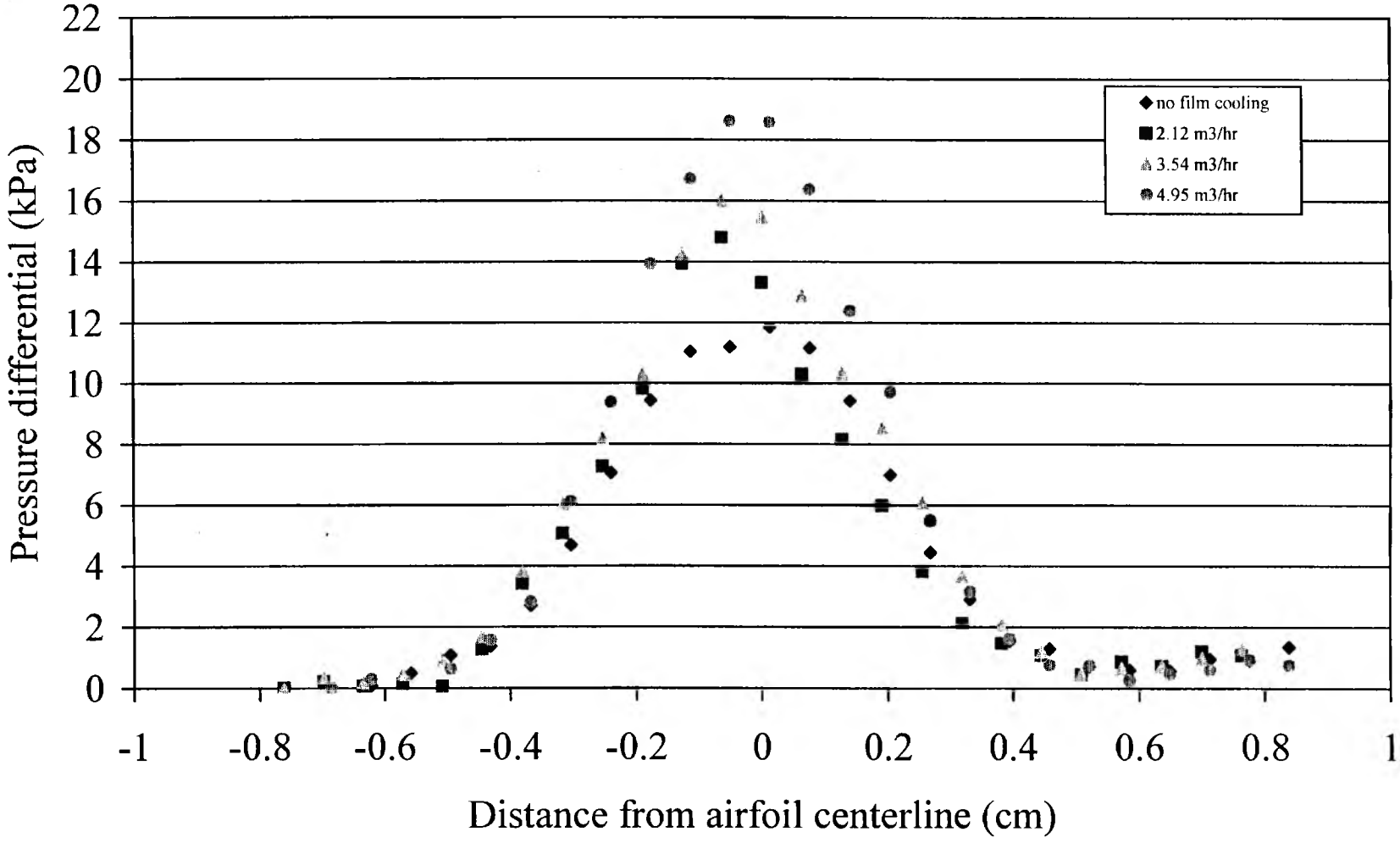

Figure 5.3 Pressure differential between test section inlet and outlet
(Blade 3, "ambient" film cooling; aerodynamic losses).

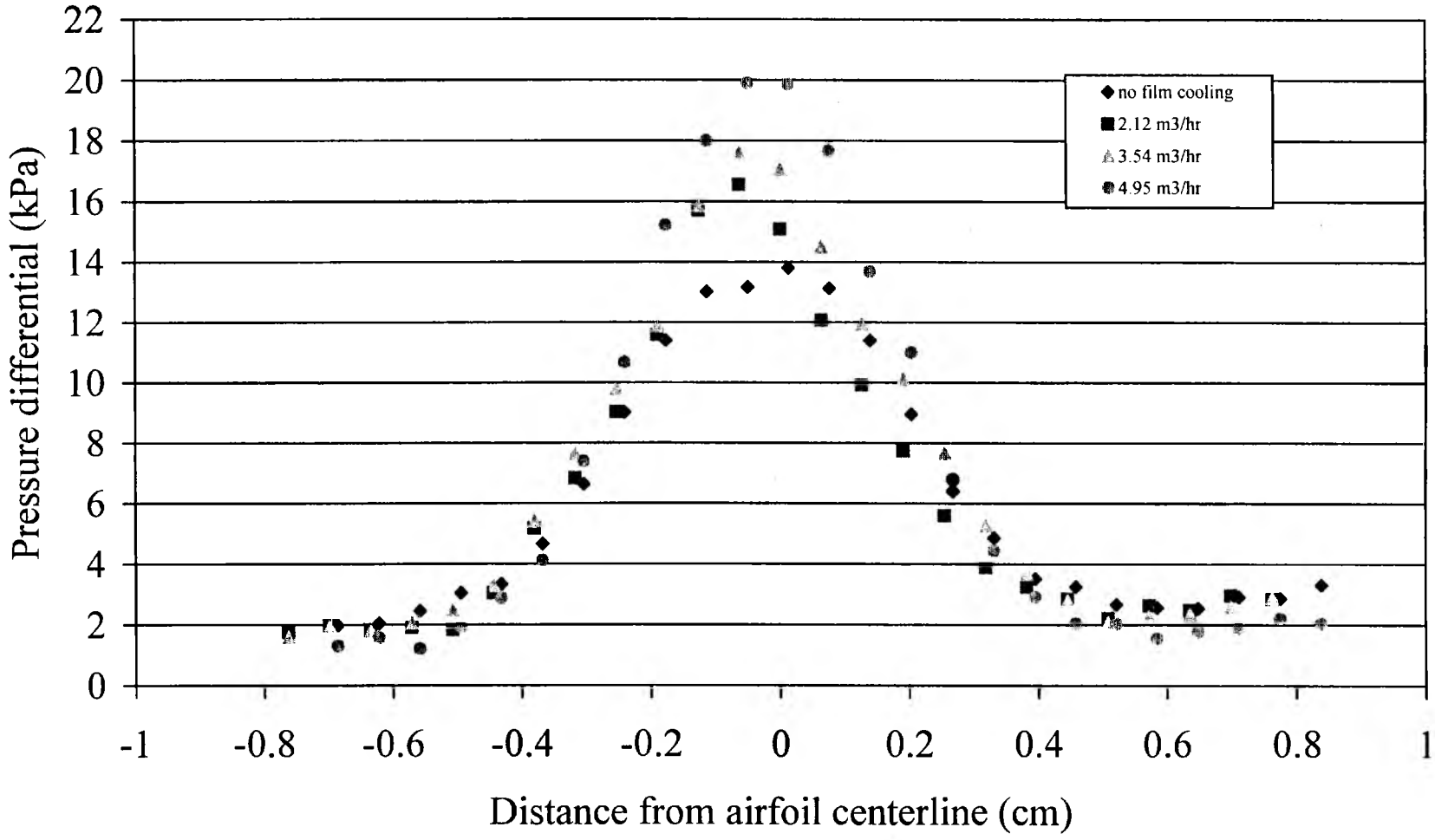

Figure 5.4 Pressure differential between test section inlet and outlet
(Blade 3, "ambient" film cooling; shock wave and aerodynamic losses).

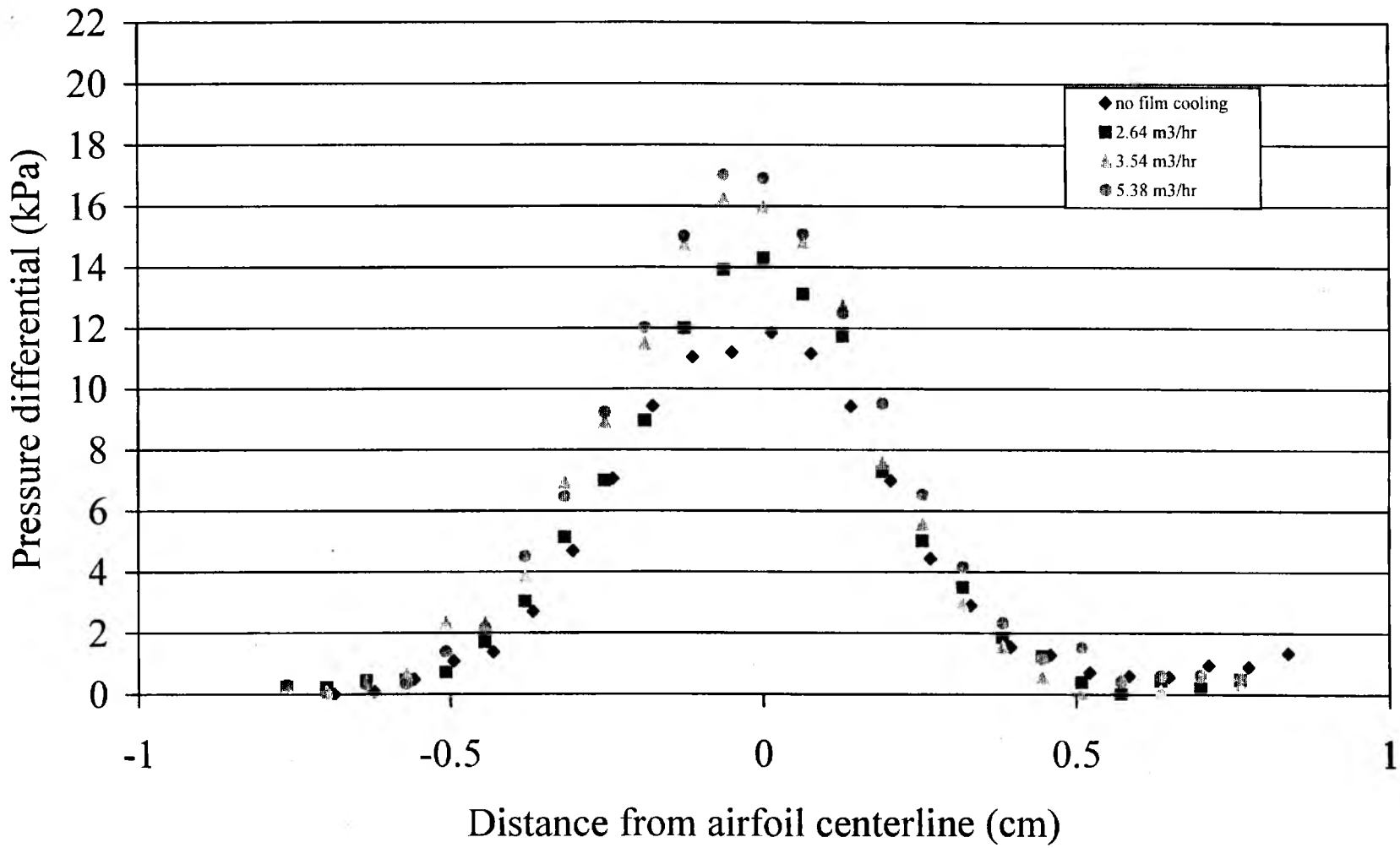

Figure 5.5 Pressure differential between test section inlet and outlet
(Blade 3, "cold" film cooling; aerodynamic losses).

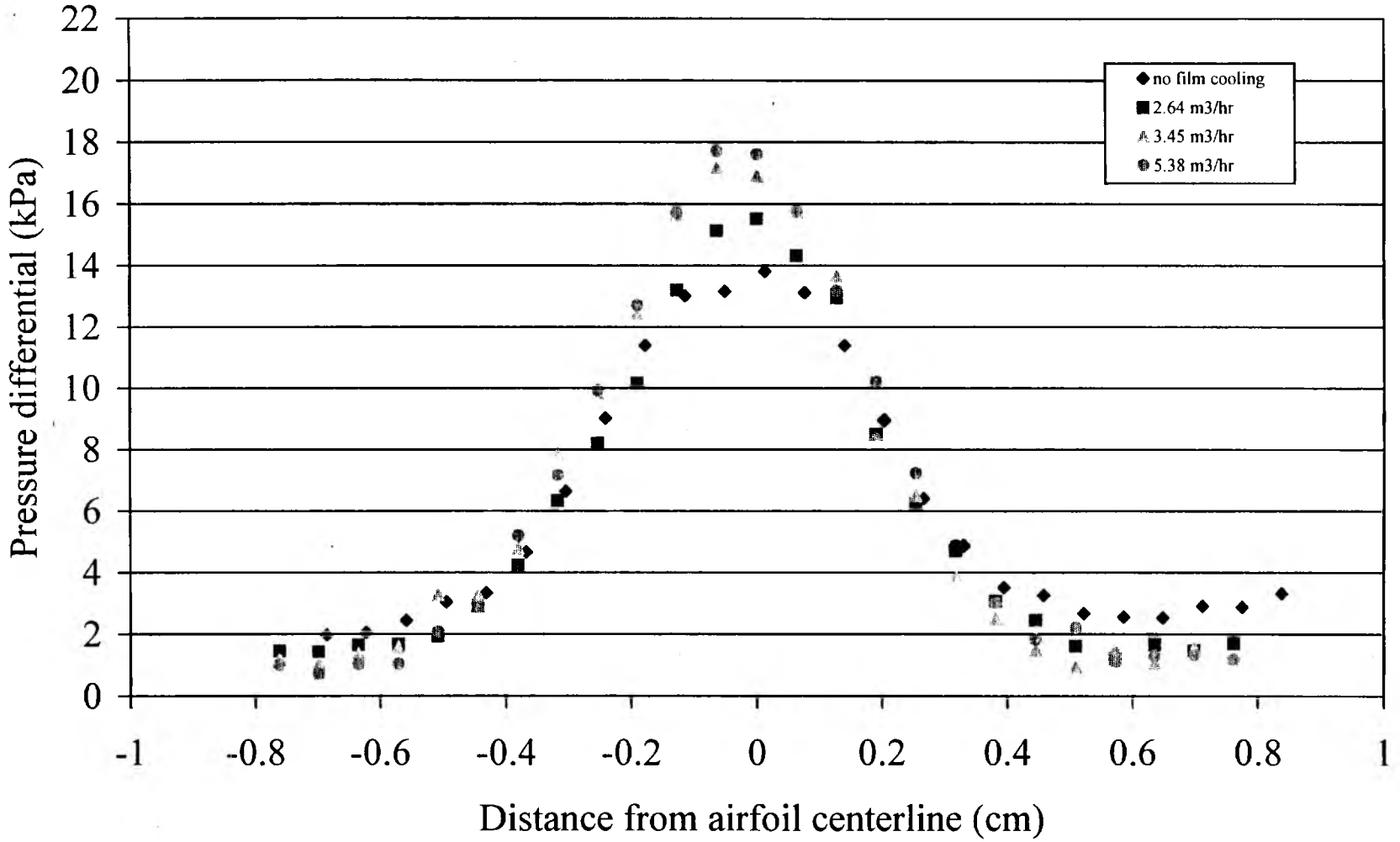

Figure 5.6 Pressure differential between test section inlet and outlet (Blade 3, "cold" film cooling; shock wave and aerodynamic losses).

5.2 Pratt and Whitney Blade 4

Table 5.2 gives the experimental conditions for Blade 4. Included is the volumetric flow rate of the film cooling, density ratios, Mach number ratios, blowing ratios, pressure ratios, and values of integrated aerodynamic loss.

5.2.1 Discharge Coefficients

Blade 4 discharge coefficients for both "ambient" and "cold" film cooling are given in Figures 5.7 and 5.8, which show values for three different pressure ratios for "ambient" and "cold" film cooling with and without freestream cross flow. All baseline data with "no cross flow" are obtained with "ambient" film cooling. "Ambient" film cooling discharge coefficients match baseline data at high pressure ratios but are somewhat lower as the pressure ratios get smaller. "Cold" film cooling discharge coefficients approach baseline data at high pressure ratios but are somewhat lower as the pressure ratios get smaller. Discharge coefficients shown in these two figures range from 0.54 to 0.78. A hole diameter of 0.469 mm (0.0185 in)is used in the determination of the discharge coefficients and all other parameters in Table 5.2.

5.2.2 Wake Characteristics

Plots of the difference between inlet and exit total pressure as dependent upon distance from the airfoil centerline are given in Figures 5.9 to 5.12 for Blade 4.

Figure 5.9 shows aerodynamic losses with "ambient" film cooling. The greatest losses are measured directly behind the airfoil centerline. Loss magnitudes increase as the mass flow rate of film cooling injectant increases. Figure 5.10 includes contributions

from oblique shock waves and "ambient" film cooling. Contributions from the "shock waves" are then removed in Figure 5.9.

Figure 5.11 shows aerodynamic losses with "cold" film cooling. Figure 5.12 includes contributions from the oblique trailing edge shock waves. Such contributions are removed from data in Figures 5.9 and 5.11 by subtracting the lowest pressure from all of the pressure values. With this adjustment, freestream pressures are then the same at the test section inlet and exit in Figures 5.9 and 5.11. For both "ambient" and "cold" film cooling, the greatest losses are present at volumetric flow rates near 4.95 m^3/hr. At the same pressure ratio, the "cold" film cooling losses are slightly lower than those for "ambient" film cooling.

5.3 Comparison of Integrated Aerodynamic Losses

Figure 5.13 shows values of the integrated aerodynamic losses as dependent upon the Mach number ratio. At the same Mach number ratio, Blade 4 has larger aerodynamic losses than Blade 3. Blade 4 has about the same aerodynamic losses for "ambient" and "cold" film cooling, when compared at the same Mach number ratio. "Cold" film cooling data are slightly higher than "ambient" film cooling data (when compared at the same Mach number ratio) for Blade 3.

Table 5.2 Experimental conditions, Blade 4.

No Cooling

m3/hr	Density Ratio ρ_c/ρ_∞	Mach Ratio M_c/M_∞	Blowing Ratio m	Pressure Ratio P_{oc}/P_∞	Integral Value of Aerodynamic Losses (N/cm)
0	--	--	--	--	0.753

Ambient Tests

m3/hr	Density Ratio ρ_c/ρ_∞	Mach Ratio M_c/M_∞	Blowing Ratio m	Pressure Ratio P_{oc}/P_∞	Integral Value of Aerodynamic Losses (N/cm)
2.41	0.838	0.487	0.25	1.197	0.919
3.54	0.867	0.635	0.39	1.357	0.907
4.95	0.950	0.932	0.70	1.876	0.963

Cold Tests

m3/hr	Density Ratio ρ_c/ρ_∞	Mach Ratio M_c/M_∞	Blowing Ratio m	Pressure Ratio P_{oc}/P_∞	Integral Value of Aerodynamic Losses (N/cm)
2.41	1.032	0.434	0.24	1.153	0.866
3.54	1.127	0.596	0.39	1.305	0.877
4.95	1.223	0.803	0.61	1.607	0.942

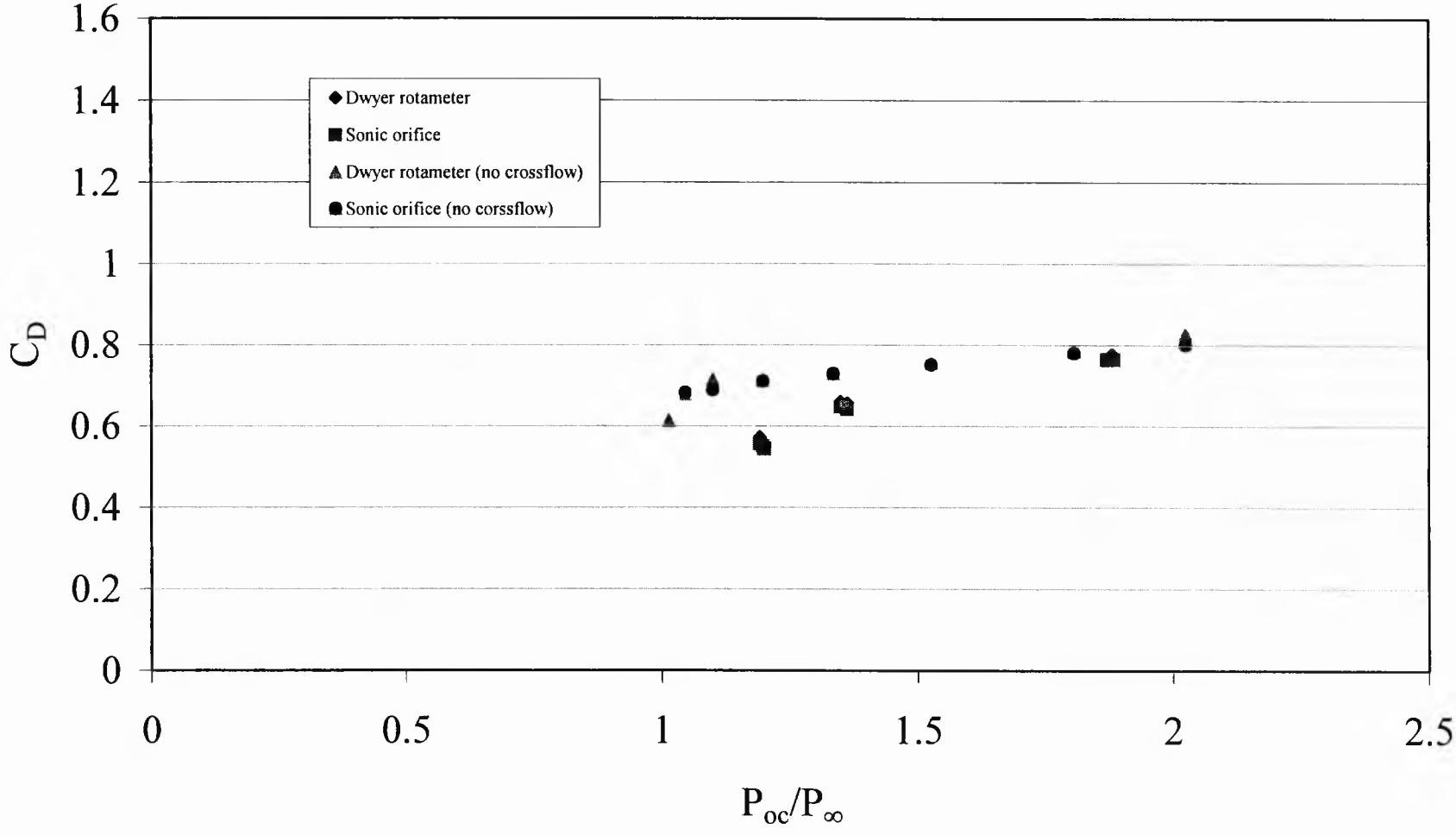

Figure 5.7 Discharge coefficients versus pressure ratios for Blade 4 ("ambient" film cooling).

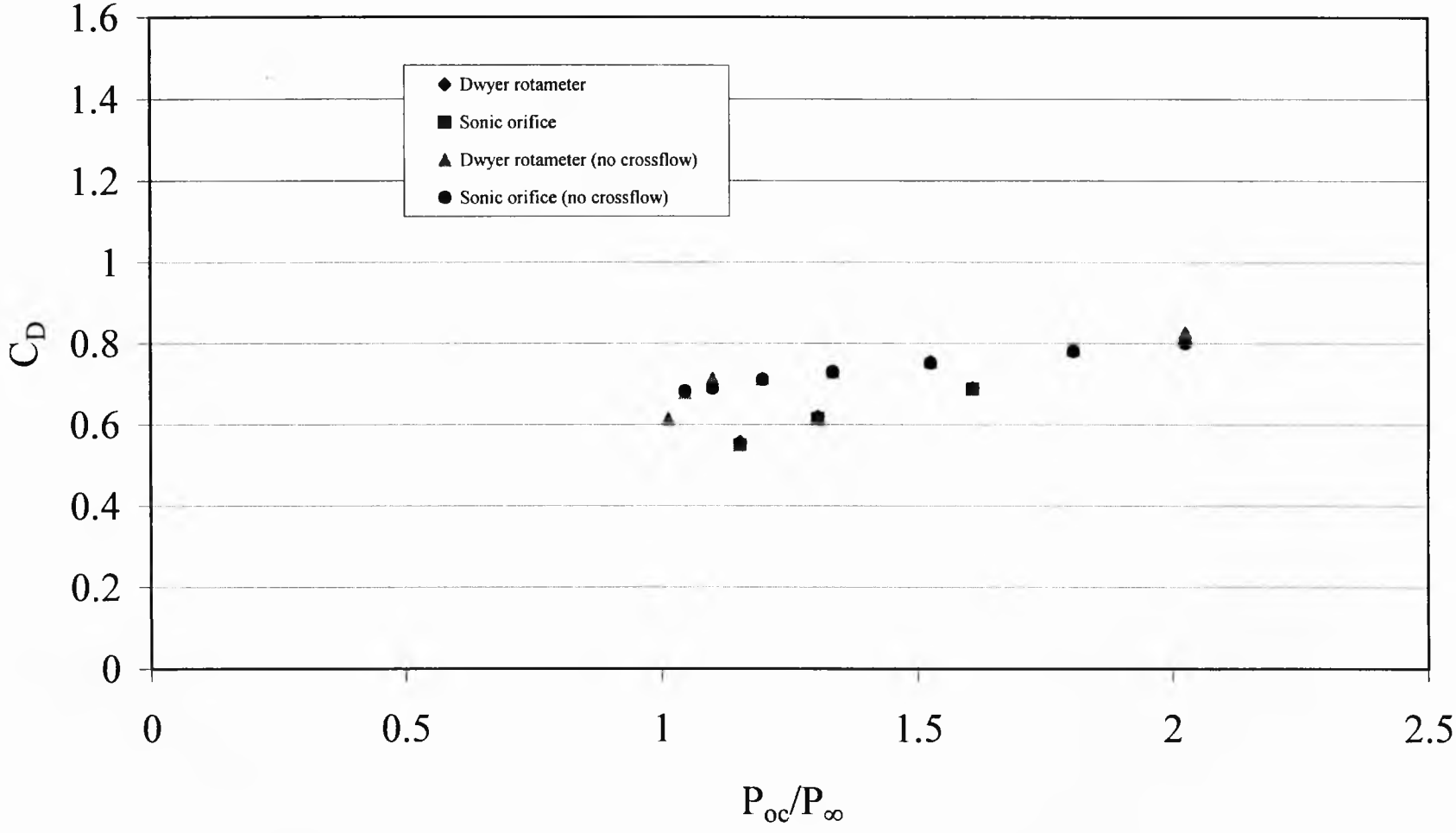

Figure 5.8 Discharge coefficients versus pressure ratios for Blade 4 ("cold" film cooling).

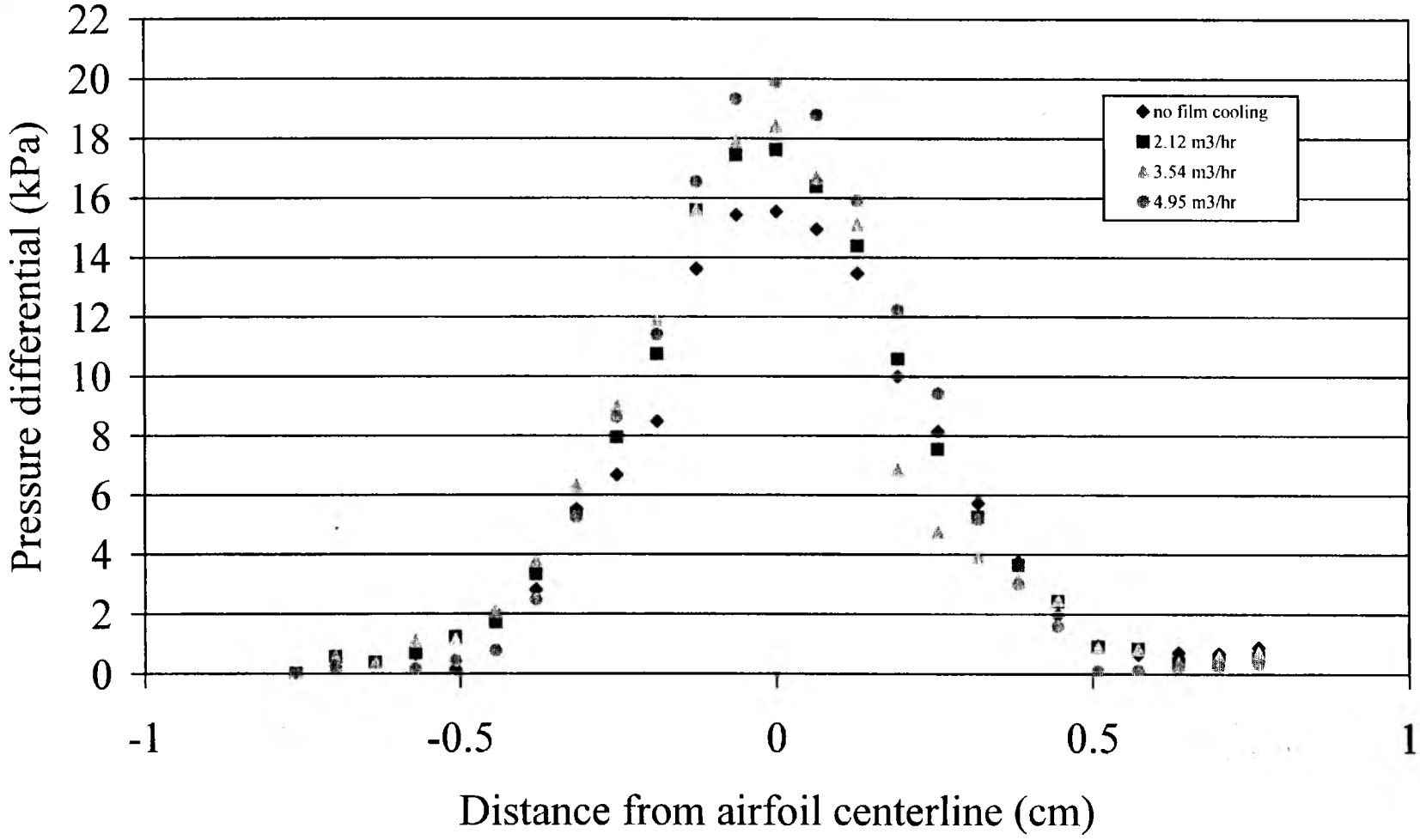

Figure 5.9 Pressure differential between test section inlet and outlet
(Blade 4, "ambient" film cooling, aerodynamic losses).

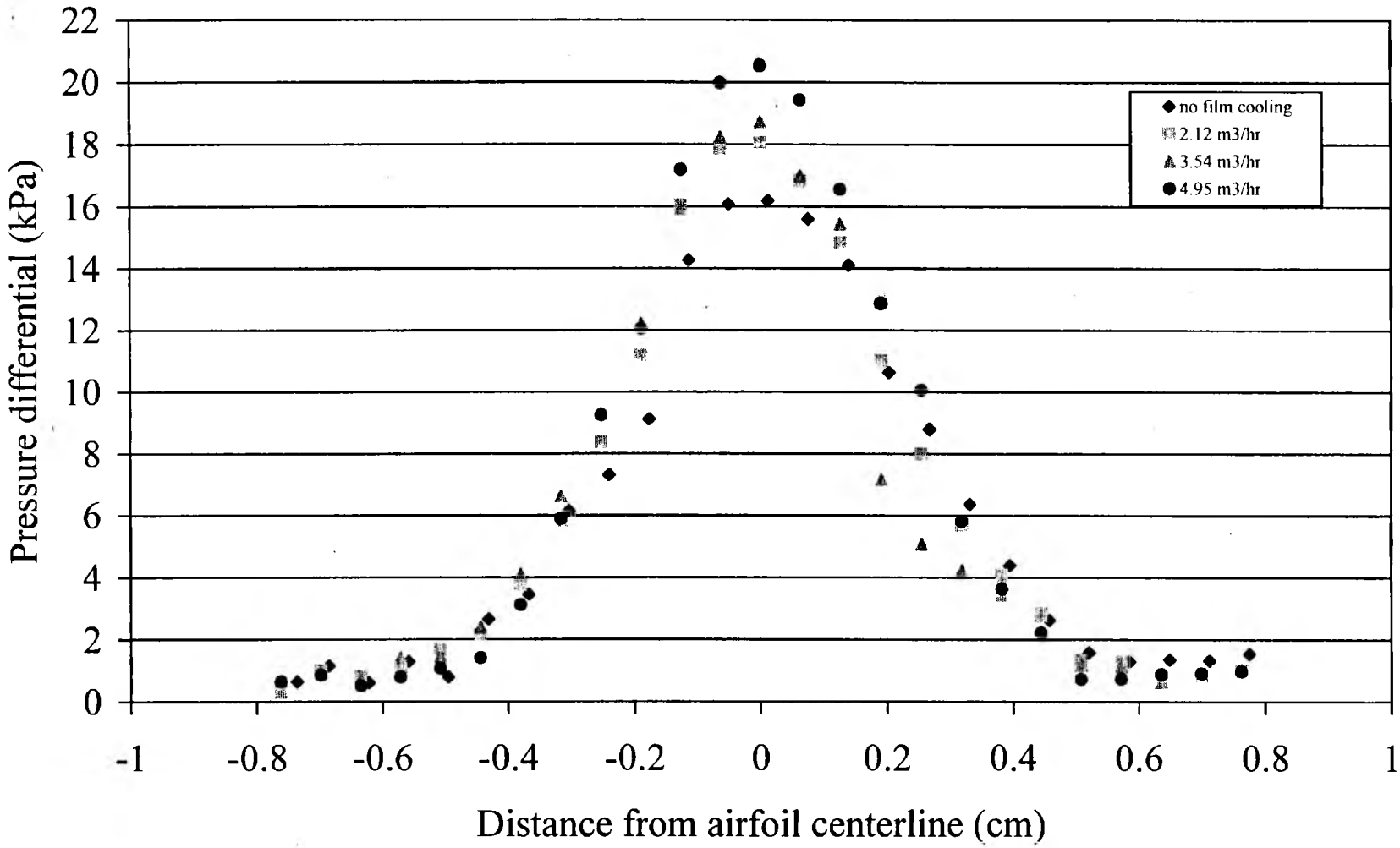

Figure 5.10 Pressure differential between test section inlet and outlet
(Blade 4, "ambient" film cooling, shock wave and aerodynamic losses).

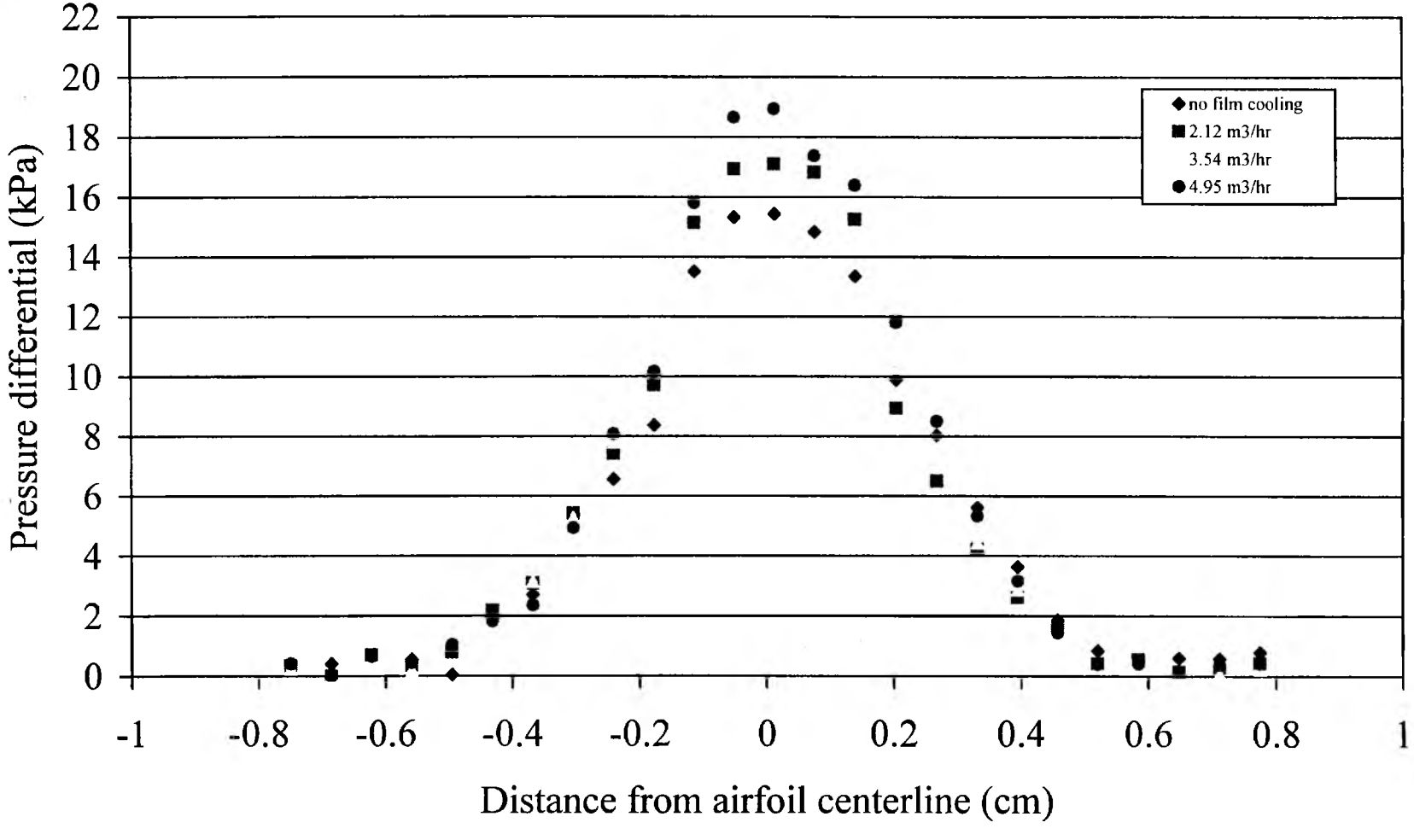

Figure 5.11 Pressure differential between test section inlet and outlet
(Blade 4, "cold" film cooling, aerodynamic losses).

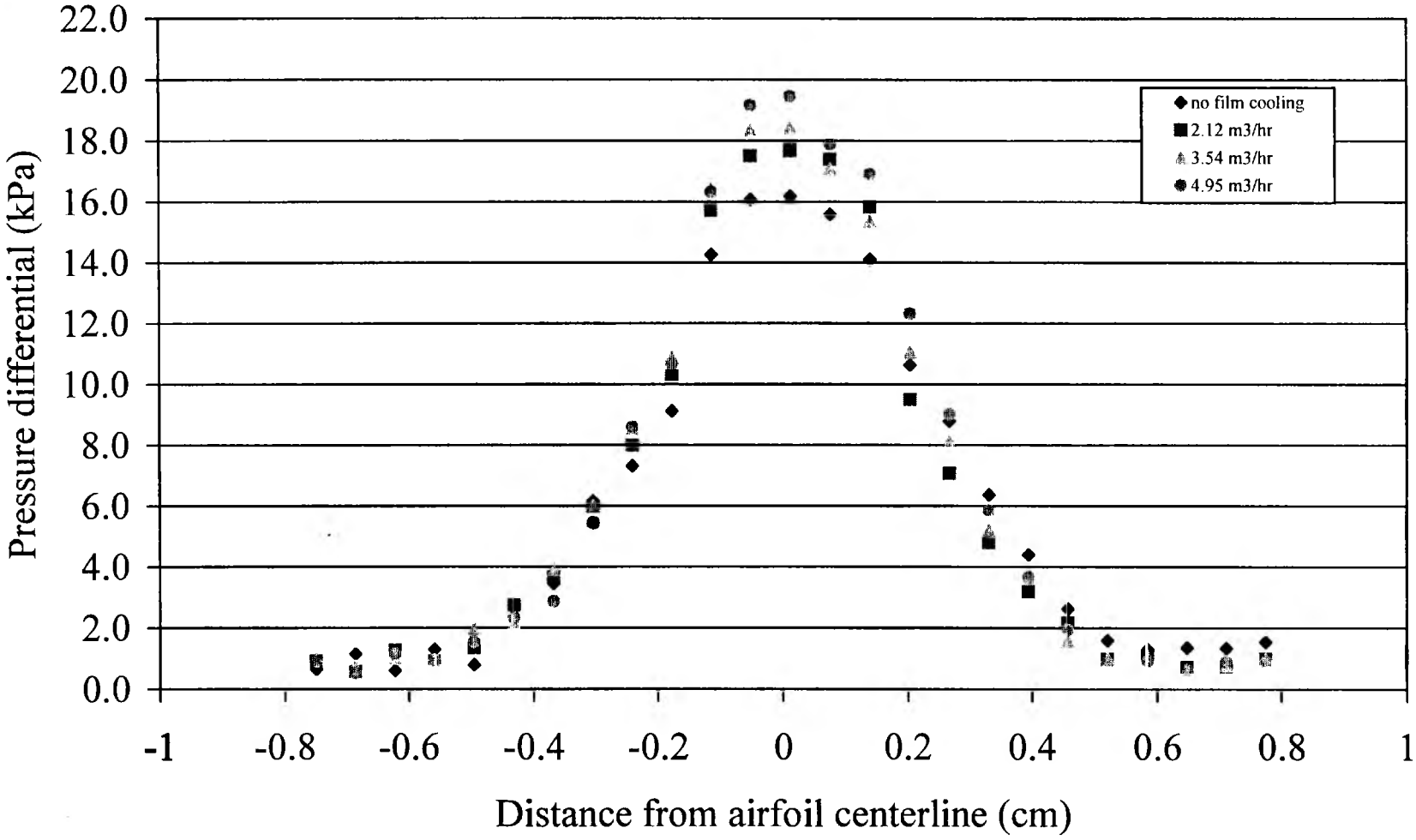

Figure 5.12 Pressure differential between test section inlet and outlet
(Blade 4, "cold" film cooling, shock wave and aerodynamic lossses).

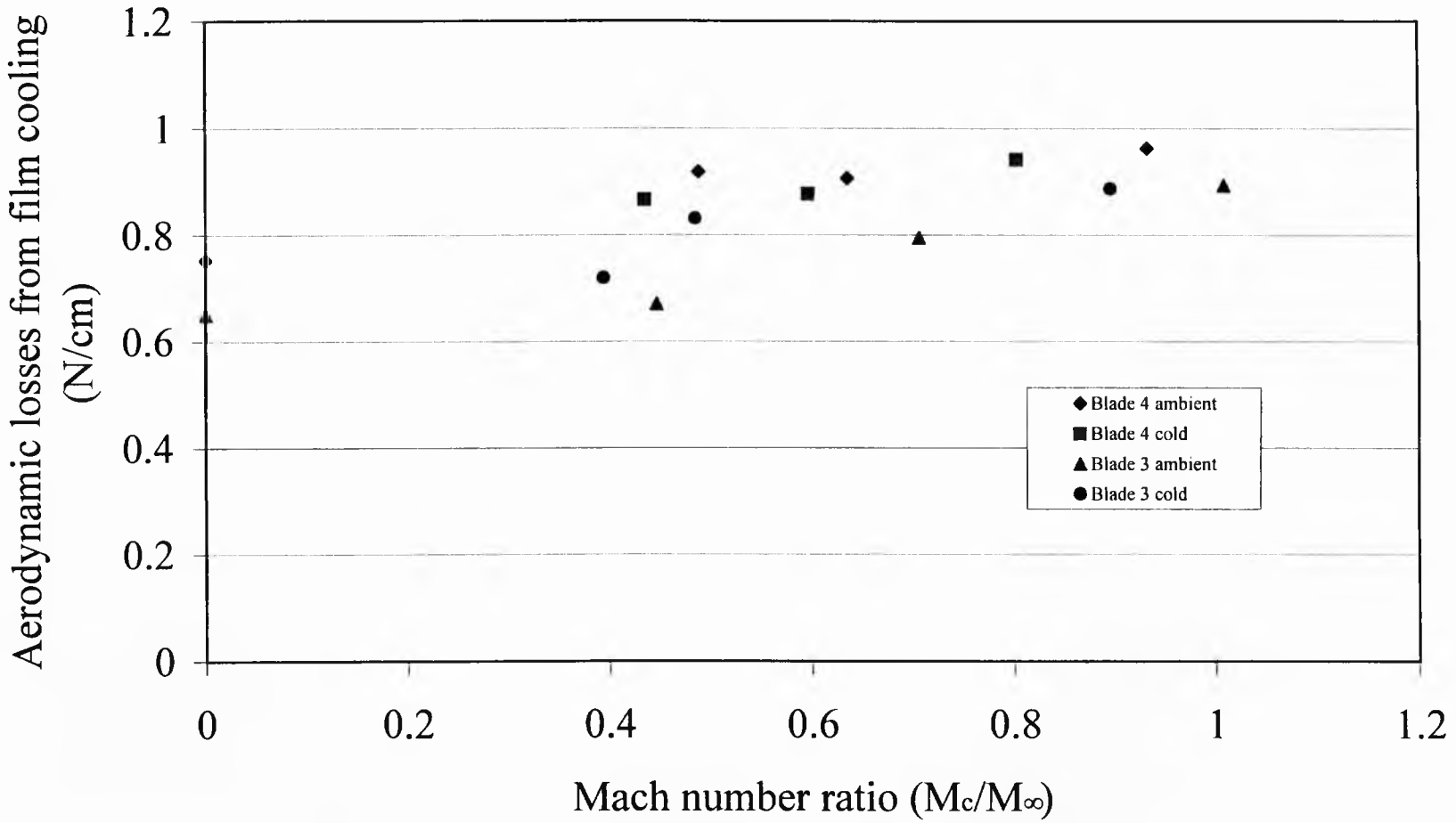

Figure 5.13 Mach ratio versus aerodynamic losses from film cooling.

CHAPTER 6

SUMMARY AND CONCULUSIONS

Aerodynamic losses and discharge coefficients are obtained for two different Pratt and Whitney axisymetric turbine airfoils with film cooling holes. Blade 3 results are given for three different blowing ratios, between 0.42 and 1.28. The pressure ratios range between 1.18 and 2.07 for the "ambient" tests and between 1.12 and 1.78 for the "cold" tests. The density ratio ranges between 0.840 and 0.973 for the "ambient" tests and 1.130 and 1.330 for the "cold" tests. Blade 4 results are give for three different blowing ratios, between 0.248 and 0.697. The pressure ratios range between 1.197 and 1.876 for the "ambient" tests and between 1.153 and 1.607 for the "cold" tests. The density ratio ranges between 0.838 and 0.95 for the "ambient" tests and 1.032 and 1.223 for the "cold" tests.

Results of qualification tests of the Transonic Wind Tunnel are also given. These include test section inlet uniformity, flow variation with time, Schlerien images of the test section flow, and the Mach number distribution along the surface of the airfoil. All indicate satisfactory test section and wind tunnel preformance.

The integrated aerodynamic losses for Blade 3 range between .0383 and 0.51 for the "ambient" tests and between 0.411 and 0.507 for the "cold" tests. For Blade 4, the integrated aerodynamic losses range from 0.525 and 0.55 for the "ambient" tests and 0.495 and 0.538 for the "cold" tests. Integrated aerodynamic losses are generally lower

with "cold" injection than with "ambient" injection for Blade 3. Blade 3 gives lower integrated aerodynamic losses compared to Blade 4 when compared at the same Mach number ratio. This is attributed to the different film hole geometries of the blades.

The discharge coefficients associated with the film holes on Blade 3 range from 0.94 to 1.3 for "ambient" tests and 1.07 to 1.3 for "cold" tests. The discharge coefficients associated with the film holes on Blade 4 range from 0.54 to 0.78 for "ambient" tests and 0.55 to 0.80 for "cold" tests. Hole diameters used to calculate discharge coefficients are 0.381 mm and 0.469 mm for Blades 3 and 4, respectively. These diameters account for some discharge coefficient values greater than one. In all cases, discharge coefficients increase as the pressure ratio increases, and discharge coefficients measured with freestream cross flow are generally lower than values measured with no freestream cross flow for pressure ratios less than about 1.5, when compared at the same pressure ratio.

APPENDIX A

PROGRAMS

A.1 BLP1 and BLPAN1

BLP1 acquires pressures from a pressure tap blade in order to be used in BLPAN1 which calculates the Mach number distribution along the blade surface.

A.2 BTB7 and BTBAN7B

BTB7 is used when no film cooling is being injected through the film cooling holes. It acquires pressures and temperatures at various places in the test section and traverses the pitot-static probe at the test section exit through the blade wake. BTBAN7B reduces the data that is taken with BTB7.

A.3 DB7 and VEC10

DB7 is used when film cooling is being injected through the film cooling holes. It acquires pressures and temperatures at various places in the test section and traverses the pitot-static probe at the test section exit through the blade wake. VEC10 reduces the data that is taken with DB7

A.4 DISCOEF and DISCOEFAN

DISCOEF is used to determine the discharge coefficients of a blade with no cross flow. It collects temperatures and pressures to be used by DISCOEFAN, which analyzes the data.

A.5 IG and IGAN2

IG is used to collect pressures at the test section inlet. IGAN2 reduces the data to receive the Mach number at the test section inlet.

A.6 SONORF and SONORFAN

SONORF collects pressures and temperatures to be used in SONORFAN. SONORFAN calculates the mass flow rates through the sonic orifice, Dwyer rotameter, and a dry gas meter.

A.7 SVUP and SVDOWN

SVUP moves the traversing pitot-static probe located at the test section exit up. SVDOWN moves the probe down. These programs are used to position the probe at a starting location for blow down tests.

APPENDIX B

DATA FILES

Filename	Operating System	Flow Rate	Date Created
Test section Inlet Profiles			
IGT1204P	HP-Basic	NA	4 December 1997
IGT1204Q	HP-Basic	NA	4 December 1997
1204PDOS	DOS	NA	4 December 1997
1204QDOS	DOS	NA	4 December 1997
IG1209U4	HP-Basic	NA	9 December 1997
IG1209U4	HP-Basic	NA	9 December 1997
IG1209U3	HP-Basic	NA	9 December 1997
IG1209U2	HP-Basic	NA	9 December 1997
IG1209U1	HP-Basic	NA	9 December 1997
IG120900	HP-Basic	NA	9 December 1997
IG1209D1	HP-Basic	NA	9 December 1997
IG1209D2	HP-Basic	NA	9 December 1997
IG1209D3	HP-Basic	NA	9 December 1997
IG1209D4	HP-Basic	NA	9 December 1997
Mach Number Distribution over the Blade Surface			
M1212D1	HP-Basic	NA	12 December 1997
M1212D1A	HP-Basic	NA	12 December 1997
M1212D2	HP-Basic	NA	12 December 1997
M1212D2A	HP-Basic	NA	12 December 1997
M1212S1	HP-Basic	NA	12 December 1997
M1212S1A	HP-Basic	NA	12 December 1997

Filename	Operating System	Flow Rate	Date Created
M1212S2	HP-Basic	NA	12 December 1997
M1212S2A	HP-Basic	NA	12 December 1997
Pratt and Whitney Blade 3			
C0305050	HP-Basic	50 SCFH	5 March 1997
C0305070	HP-Basic	70 SCFH	5 March 1997
C0305100	HP-Basic	100 SCFH	5 March 1997
C0305125	HP-Basic	125 SCFH	5 March 1997
C0305150	HP-Basic	150 SCFH	5 March 1997
C0305180	HP-Basic	180 SCFH	5 March 1997
B30216A	HP-Basic	NA	16 January 1997
B30216B	HP-Basic	NA	16 January 1997
B30216C	HP-Basic	NA	16 January 1997
B30216D	HP-Basic	NA	16 January 1997
B30216E	HP-Basic	NA	16 January 1997
0216A	DOS	NA	16 January 1997
0216B	DOS	NA	16 January 1997
0216C	DOS	NA	16 January 1997
0216D	DOS	NA	16 January 1997
0216E	DOS	NA	16 January 1997
B3C0302A	HP-Basic	173 SCFH	2 March 1997
B3C0302B	HP-Basic	170 SCFH	2 March 1997
B3C0302C	HP-Basic	172 SCFH	2 March 1997

Filename	Operating System	Flow Rate	Date Created
B3C0302D	HP-Basic	173 SCFH	2 March 1997
B3C0302E	HP-Basic	172 SCFH	2 March 1997
DOS0302A	DOS	173 SCFH	2 March 1997
DOS0302B	DOS	170 SCFH	2 March 1997
DOS0302C	DOS	172 SCFH	2 March 1997
DOS0302D	DOS	173 SCFH	2 March 1997
DOS0302E	DOS	172 SCFH	2 March 1997
B3C0303A	HP-Basic	122 SCFH	3 March 1997
B3C0303B	HP-Basic	123 SCFH	3 March 1997
B3C0303C	HP-Basic	123 SCFH	3 March 1997
B3C0303D	HP-Basic	122 SCFH	3 March 1997
B3C0303E	HP-Basic	122 SCFH	3 March 1997
DOS0303A	DOS	122 SCFH	3 March 1997
DOS0303B	DOS	123 SCFH	3 March 1997
DOS0303C	DOS	112 SCFH	3 March 1997
DOS0303D	DOS	122 SCFH	3 March 1997
DOS0303E	DOS	122 SCFH	3 March 1997
B3C0304A	HP-Basic	78 SCFH	4 March 1997
B3C0304B	HP-Basic	77 SCFH	4 March 1997
B3C0304C	HP-Basic	77 SCFH	4 March 1997
B3C0304D	HP-Basic	78 SCFH	4 March 1997
B3C0304E	HP-Basic	78 SCFH	4 March 1997

Filename	Operating System	Flow Rate	Date Created
DOS0304A	DOS	78 SCFH	4 March 1997
DOS0304B	DOS	77 SCFH	4 March 1997
DOS0304C	DOS	77 SCFH	4 March 1997
DOS0304D	DOS	78 SCFH	4 March 1997
DOS0304E	DOS	78 SCFH	4 March 1997
B3C0318A	HP-Basic	120 SCFH	18 March 1997
B3C0318B	HP-Basic	119 SCFH	18 March 1997
B3C0318C	HP-Basic	120 SCFH	18 March 1997
B3C0318D	HP-Basic	119 SCFH	18 March 1997
B3C0318E	HP-Basic	121 SCFH	18 March 1997
DOS0318A	DOS	120 SCFH	18 March 1997
DOS0318B	DOS	119 SCFH	18 March 1997
DOS0318C	DOS	120 SCFH	18 March 1997
DOS0318D	DOS	119 SCFH	18 March 1997
DOS0318E	DOS	121 SCFH	18 March 1997
B3C0320A	HP-Basic	93 SCFH	20 March 1997
B3C0320B	HP-Basic	90 SCFH	20 March 1997
B3C0320C	HP-Basic	91 SCFH	20 March 1997
B3C0320D	HP-Basic	90 SCFH	20 March 1997
B3C0320E	HP-Basic	90 SCFH	20 March 1997
DOS0320A	DOS	93 SCFH	20 March 1997
DOS0320B	DOS	90 SCFH	20 March 1997

Filename	Operating System	Flow Rate	Date Created
DOS0320C	DOS	91 SCFH	20 March 1997
DOS0320D	DOS	90 SCFH	20 March 1997
DOS0320E	DOS	90 SCFH	20 March 1997
B3C0320F	HP-Basic	191 SCFH	20 March 1997
B3C0320G	HP-Basic	192 SCFH	20 March 1997
B3C0320H	HP-Basic	192 SCFH	20 March 1997
B3C0320I	HP-Basic	191 SCFH	20 March 1997
B3C0320J	HP-Basic	190 SCFH	20 March 1997
DOS0320F	DOS	191 SCFH	20 March 1997
DOS0320G	DOS	192 SCFH	20 March 1997
DOS0320H	DOS	192 SCFH	20 March 1997
DOS0320I	DOS	191 SCFH	20 March 1997
DOS0320J	DOS	190 SCFH	20 March 1997
Pratt and Whitney Blade 4			
CD0709A	HP-Basic	199 SCFH	9 July 1997
CD0709B	HP-Basic	175 SCFH	9 July 1997
CD0709C	HP-Basic	150 SCFH	9 July 1997
CD0709D	HP-Basic	125 SCFH	9 July 1997
CD0709E	HP-Basic	100 SCFH	9 July 1997
CD0709F	HP-Basic	75 SCFH	9 July 1997
CD0709G	HP-Basic	50 SCFH	9 July 1997
CD0709H	HP-Basic	25 SCFH	9 July 1997

Filename	Operating System	Flow Rate	Date Created
B40709Z	HP-Basic	NA	9 July 1997
B40709Y	HP-Basic	NA	9 July 1997
B40709X	HP-Basic	NA	9 July 1997
B40709W	HP-Basic	NA	9 July 1997
B40709V	HP-Basic	NA	9 July 1997
B40709G	HP-Basic	185 SCFH	9 July 1997
B40709H	HP-Basic	185 SCFH	9 July 1997
B40709I	HP-Basic	186 SCFH	9 July 1997
B40709J	HP-Basic	185 SCFH	9 July 1997
B40709K	HP-Basic	185 SCFH	9 July 1997
DOS0709G	DOS	185 SCFH	9 July 1997
DOS0709H	DOS	185 SCFH	9 July 1997
DOS0709I	DOS	186 SCFH	9 July 1997
DOS0709J	DOS	185 SCFH	9 July 1997
DOS0709K	DOS	185 SCFH	9 July 1997
B40709L	HP-Basic	123 SCFH	9 July 1997
B40709M	HP-Basic	123 SCFH	9 July 1997
B40709N	HP-Basic	122 SCFH	9 July 1997
B40709O	HP-Basic	123 SCFH	9 July 1997
B40709P	HP-Basic	122 SCFH	9 July 1997
DOS0709L	DOS	123 SCFH	9 July 1997
DOS0709M	DOS	123 SCFH	9 July 1997

Filename	Operating System	Flow Rate	Date Created
DOS0709N	DOS	122 SCFH	9 July 1997
DOS0709O	DOS	123 SCFH	9 July 1997
DOS0709P	DOS	122 SCFH	9 July 1997
B40709Q	HP-Basic	85 SCFH	9 July 1997
B40709R	HP-Basic	84 SCFH	9 July 1997
B40709S	HP-Basic	84 SCFH	9 July 1997
B40709T	HP-Basic	83 SCFH	9 July 1997
B40709U	HP-Basic	84 SCFH	9 July 1997
DOS0709Q	DOS	85 SCFH	9 July 1997
DOS0709R	DOS	84 SCFH	9 July 1997
DOS0709S	DOS	84 SCFH	9 July 1997
DOS0709T	DOS	83 SCFH	9 July 1997
DOS0709U	DOS	84 SCFH	9 July 1997
B4C0709A	HP-Basic	174 SCFH	9 July 1997
B4C0709B	HP-Basic	177 SCFH	9 July 1997
B4C0709C	HP-Basic	177 SCFH	9 July 1997
B4C0709D	HP-Basic	178 SCFH	9 July 1997
B4C0709E	HP-Basic	176 SCFH	9 July 1997
DC0709A	DOS	174 SCFH	9 July 1997
DC0709B	DOS	177 SCFH	9 July 1997
DC0709C	DOS	177 SCFH	9 July 1997
DC0709D	DOS	178 SCFH	9 July 1997

Filename	Operating System	Flow Rate	Date Created
DC0709E	DOS	176 SCFH	9 July 1997
B4C0709F	HP-Basic	128 SCFH	9 July 1997
B4C0709G	HP-Basic	132 SCFH	9 July 1997
B4C0709H	HP-Basic	128 SCFH	9 July 1997
B4C0709I	HP-Basic	121 SCFH	9 July 1997
B4C0709J	HP-Basic	125 SCFH	9 July 1997
DC0709F	DOS	128 SCFH	9 July 1997
DC0709G	DOS	132 SCFH	9 July 1997
DC0709H	DOS	128 SCFH	9 July 1997
DC0709I	DOS	121 SCFH	9 July 1997
DC0709J	DOS	125 SCFH	9 July 1997
B4C0709K	HP-Basic	85 SCFH	9 July 1997
B4C0709L	HP-Basic	84 SCFH	9 July 1997
B4C0709M	HP-Basic	87 SCFH	9 July 1997
B4C0709N	HP-Basic	84 SCFH	9 July 1997
B4C0709O	HP-Basic	83 SCFH	9 July 1997
DC0709K	DOS	85 SCFH	9 July 1997
DC0709L	DOS	84 SCFH	9 July 1997
DC0709M	DOS	87 SCFH	9 July 1997
DC0709N	DOS	84 SCFH	9 July 1997
DC0709O	DOS	83 SCFH	9 July 1997

REFERENCES

Ames, F. E., and Plesniak, M. W., 1997, "The Influence of Large-Scale, High-Intensity Turbulence on Vane Aerodynamic Losses, Wake Growth, and the Exit Turbulence Parameters," *Transactions of the ASME*, Vol. 119, April, pp. 182-192.

Brittingham R. A., and Leylek J. A., 1997, "A Detailed Analysis of Film Cooling Physics Part IV: Compound- Angle Injection With Shaped Holes," *ASME Paper* No. 97-GT-272.

Hay, N., and Lampard, D., 1995, "The Discharge Coefficient of Flared Film Cooling Holes," *ASME Paper* No. 95-GT-15.

Hay, N., Henshall, S. E., and Manning, A., 1992, "Discharge Coefficients of Holes Angled to the Flow Direction," *Journal of Turbomachinery*, Vol. 115, January, pp. 92-96.

Hay, N., Lampard, D., and Benmansour, S., 1982, "Effect of Crossflow on the Discharge Coefficient of Film Cooling Holes," *ASME Paper* No. 82-GT-147.

Hymas, D. G., and Leylek, J. H., 1997, "A Detailed Analysis of Film Cooling Physics Part III: Streamwise Injection with Shaped Holes," *ASME Paper* No. 97-GT-271.

Kapteijn, C., Amecke, J., and Michelassi, V., 1994, "Aerodynamic Performance of a Transonic Turbine Guide Bane with Trailing Edge Coolant Ejection: Part I – Experimental Approach," *ASME Paper* No. 94-GT-288.

McGovern, K. T., and Leylek J. H., 1997, "A Detailed Analysis of Film Cooling Physics Part II. Compound-Angle Injection with Cylindrical Holes," *ASME Paper* No. 97-GT-270.

Mee, D. J., Baines, N. C., Oldfield, M. L. G., and Dickens, T. E., 1992, "An Examination of the Contributions to Loss on a Transonic Turbine Blade in Cascade," *Journal of Turbomachinery*, Vol. 114, January, pp. 155-162.

Moffat, R. J., 1962, "Gas Temperature Measurements," *Temperature- Its Measurement and Control in Science and Industry*, Volume 3, Part 2, Chapter 3, Reinhold, New York.

Thole, K., Gritsch, M., Schulz, A., and Wittig, S., 1996, "Flowfield Measurments for Film-Cooling Holes with Expanded Exits," *ASME Paper* No. 96-GT-174.

Vlasic, E. P., Grigis, S., and Moustapha, S. H., 1995, "The Design and Performance of a High Work Research Turbine," *ASME Paper* No. 95-GT-233.

Walters, D. K., and Leylek, J. H., 1997, "A Detailed Analysis of Film Cooling Physics Part I: Streamwise Injection with Cylindrical Holes," *ASME Paper* No. 96-GT-269.

Wittig, S., Schultz, A., Gritsch, M., and Thole, K. A., 1996, "Transonic Film-Cooling Investigation: Effects of Hole Shape and Orientations," *ASME Paper* No. 96-GT-222.